https://doi.org/10.5194/essd-2026-471
Preprint. Discussion started: 24 August 2026

Open Access Earth System Science Data Discussions

Thirteen Winters (2012–2025) of Penetration-Aware Arctic Sea-Ice Emissivity and Emission Temperature from AMSR2

Eui-Jong Kang[1], Byung-Ju Sohn[1,2], Hwan-Jin Song[3], Wonho Kim[4], Chao Liu[2]

[1]School of Earth and Environmental Sciences, Seoul National University (SNU), Seoul, South Korea
[2]School of Remote Sensing and Geomatics Engineering, Nanjing University of Information Science and Technology (NUIST), Nanjing, China
[3]Department of Atmospheric Sciences, Kyungpook National University (KNU), Daegu, South Korea
[4]Korea Institute of Atmospheric Prediction Systems (KIAPS), Seoul, South Korea

Correspondence to: Byung-Ju Sohn (sohn@snu.ac.kr)

Abstract. Passive microwave observations enable long-term, all-weather monitoring of Arctic sea ice, but their physical interpretation depends on how surface emission is represented. In conventional satellite emissivity products, emissivity is typically retrieved under a skin-emission assumption, even though low-frequency microwave radiation over sea ice can originate from a deeper, non-isothermal subsurface layer. This study presents a new satellite-derived dataset of low-frequency sea-ice emissivity representative of the microwave-emitting layer and the corresponding emission temperature for wintertime Arctic sea ice. The dataset is generated using a simulation-trained retrieval framework in which penetration-aware sea-ice surface emission parameters are combined with reanalysis atmospheric profiles in radiative transfer calculations to construct forward-consistent training data, and neural-network inversion models are trained separately for emissivity and emission temperature to retrieve each variable independently from top-of-atmosphere brightness temperatures.

With the developed algorithm applied to Advanced Microwave Scanning Radiometer 2 (AMSR2) observations, a 13-winter record (2012/2013–2024/2025) of penetration-aware emissivity and emission temperature is produced over the Arctic Ocean north of 70°N under high sea-ice concentration (Kang, 2026; https://tinyurl.com/5n6843r8). Because neither emissivity nor emission temperature has a direct observational reference, the retrieval is evaluated in observation space via radiative-transfer closure. Brightness temperatures forward-simulated from the retrieved parameters agree closely with AMSR2 observations across all winters ($r \approx 0.99$, spread of about 1 K), demonstrating radiative consistency despite training on simulation-based data. Comparable agreement is obtained at the 23.8 GHz horizontally polarized channel, which is not used in the retrieval, supporting cross-channel physical consistency. The dataset is temporally stable across winters and is intended to support radiative-transfer applications, satellite retrieval development, sea-ice characterization, and polar data assimilation.

1 Introduction

Passive microwave satellite observations have provided a long and nearly continuous record of Arctic sea-ice concentration (SIC) since the launch of the Scanning Multichannel Microwave Radiometer (SMMR) in 1978 (Gloersen and Barath, 1977).

https://doi.org/10.5194/essd-2026-471
Preprint. Discussion started: 24 August 2026

Successive microwave imagers have thereby enabled consistent, all-weather monitoring of the Arctic sea-ice cover. In low-frequency atmospheric window bands, atmospheric absorption and scattering are relatively weak, so satellite-observed top-of-atmosphere (TOA) brightness temperatures (TBs) are largely governed by surface emission (Grody, 1988). As a result, observations in these bands are highly sensitive to the physical state of snow-covered sea ice and have formed the observational foundation for a wide range of satellite-derived sea-ice products, including concentration, type, drift, edge, and thickness (Cavalieri et al., 1984; Comiso, 1986; Belchansky et al., 2004; Worby and Comiso, 2004; Lavergne et al., 2010; Lee et al., 2017; Nakata et al., 2019; Kim et al., 2022).

For microwave applications, the surface contribution is commonly described by two radiative boundary parameters: the emissivity representative of the microwave-emitting layer and the corresponding temperature of that layer (emission temperature). Over snow-covered sea ice, this emissivity reflects the bulk microphysical and structural properties of the snow/sea-ice medium from which the microwave signal emerges, while the emission temperature represents the effective thermal state of the same layer (Comiso, 1983; Mathew et al., 2009). Together, these parameters are coupled and govern how observed TBs are interpreted in subsequent applications (e.g., Al Jassar et al., 1995). Accordingly, when emissivity is used as a lower boundary condition in retrieval algorithms or radiative-transfer applications, it must be paired with the temperature that is physically consistent with the emitting layer it represents.

However, in existing satellite emissivity products, emissivity is often not consistent with the actual microwave-emitting layer. In many cases, it is derived using a top-down inversion approach (Prigent et al., 1997) that assumes that the emission originates from the surface skin and inverts the radiative transfer equation using observed TBs together with atmospheric and surface priors, such as reanalysis (e.g., Karbou et al., 2014; Bormann et al., 2017; Wang et al., 2017; Kim et al., 2023; Kilic et al., 2025). This skin-emission assumption is operationally convenient because it simplifies the surface boundary treatment (Ferraro et al., 2013). In reality, however, over sea ice covered with dry snow, low-frequency microwave radiation can penetrate from centimeters to meters into the sea ice, with penetration depth generally increasing with wavelength (Ulaby and Long, 2015). Consequently, the observed emission originates from a subsurface layer whose temperature differs from that of the surface skin.

Because the emission temperature is generally unknown, the inversion is commonly performed by prescribing the skin temperature as the lower boundary condition. Under this constraint, the retrieved emissivity compensates for the mismatch between the assumed skin temperature and the actual temperature of the emitting layer, and is therefore regarded as an effective emissivity (Kilic et al., 2025). Since the observed microwave emission originates from a heterogeneous, non-isothermal subsurface layer within the sea ice, a physically consistent interpretation of observed TBs requires emissivity together with the corresponding temperature representative of that subsurface emitting layer.

Recent studies have advanced forward-modeling frameworks that link snow/sea-ice thermodynamics with snow/sea-ice radiative transfer to diagnose penetration-aware emissivity and emission temperature in a physically consistent manner (Kang

https://doi.org/10.5194/essd-2026-471
Preprint. Discussion started: 24 August 2026

et al., 2021; 2023). These approaches indicate that microwave observations contain recoverable information on both the thermal structure and radiative properties of the subsurface emitting layer. In parallel, machine learning (ML) techniques have provided an efficient means of approximating the inverse relationship between observed TBs and underlying subsurface sea-ice state variables (Baek et al., 2023; Kang et al., 2025). Together, these developments provide the methodological basis for constructing satellite-derived records that explicitly account for microwave penetration into the snow–ice medium.

Beyond their role in microwave retrieval algorithms, emissivity (ε) and emission temperature (T_e) together provide a physically interpretable description of the Arctic sea-ice state. Unlike conventional TB contrasts or backscattering-based diagnostics, the paired variables are directly linked to the penetration-weighted emission process within the snow/sea-ice system and therefore characterize both the radiative and thermodynamic properties of the emitting layer. In this sense, the paired {ε, Te} fields can be regarded as reusable geophysical variables rather than as intermediate quantities belonging to a particular retrieval chain. Such a record can contribute to efforts to characterize the Arctic sea-ice environment as a multivariate geophysical system (Lavergne et al., 2022) and provides a common radiometric and thermodynamic reference that can be related to other independently observed properties of sea ice.

An important application can be the assimilation of microwave radiances over sea ice. In radiative-transfer observation operators, emissivity and the corresponding emission temperature define the surface contribution and therefore influence whether surface-sensitive window and weak water-vapor channels can be effectively used. The sea-ice surface boundary remains among the less well constrained components of the microwave forward operator, making observational estimates of these quantities relevant to satellite data assimilation and thus numerical weather prediction. Because microwave emissivity responds to structural properties of the snow/ice medium that also influence radar backscatter, combined analyses may further help characterize structural evolution of sea ice. Over multiple winters, the paired fields also provide a basis for examining inter-annual variability in the radiometric and thermodynamic state of Arctic sea ice.

The present record is restricted to compact winter sea ice north of 70°N under high-concentration conditions. This seasonal restriction should not be viewed simply as a consequence of the increased retrieval uncertainty associated with melt-season conditions. A long-term winter record has independent scientific value because it can be used synergistically with complementary cold-season sea-ice products, such as sea-ice age, type, and thickness, to investigate relationships among the radiometric, thermodynamic, and structural properties of Arctic sea ice. Winter is also a season in which characterization of the microwave surface boundary over snow-covered sea ice remains particularly challenging, limiting the use of surface-sensitive microwave observations in the data assimilation for numerical weather prediction (Lawrence et al., 2019). The winter record therefore targets conditions for which improved characterization of sea-ice microwave properties is especially relevant, while providing a consistent seasonal framework for comparison with other long-term sea-ice records.

Motivated by the growing capability to retrieve physically consistent emissivity and emission temperature and by the potential of these variables for broader scientific and operational applications, this study presents a new satellite-derived dataset of low-

https://doi.org/10.5194/essd-2026-471
Preprint. Discussion started: 24 August 2026

frequency sea-ice emissivity representative of the microwave-emitting layer and the corresponding temperature of that layer. We use physically based snow/sea-ice radiative boundary simulations together with atmospheric radiative-transfer modeling to construct forward-consistent training data and employ a neural-network inversion to retrieve the paired surface parameters from observed TBs. Using observations from the Advanced Microwave Scanning Radiometer 2 (AMSR2), which has provided a stable conical-scanning record since 2012, we produce a 13-winter record of penetration-aware sea-ice emissivity and emission temperature for compact Arctic sea ice north of 70°N, spanning 2012/2013 to 2024/2025. The dataset is designed not only to provide physically consistent microwave surface boundary parameters, but also to support comparative studies of Arctic sea-ice properties and the broader use of microwave observations over snow-covered sea ice.

2 Data

This section introduces the datasets used in this study and clarifies their respective roles within the overall retrieval framework. The detailed retrieval methodology is presented in Section 3. To provide context for how each dataset contributes to the workflow, we first give an overview of the data flow, followed by descriptions of the individual data sources.

2.1 Overview of the data flow

The datasets used in this study serve distinct but interconnected roles within the overall retrieval framework, as summarized schematically in Fig. 1. The final data record of sea-ice surface emission parameters $\{\varepsilon, T_e\}$ is generated by applying the trained ML-based retrieval algorithm to observed AMSR2 TOA TBs over the Arctic winter compact sea-ice region. SIC is used to define the compact-ice analysis domain and to exclude observations affected by open-water contamination. In this sense, TBs and SIC together form the observation-based inputs for generating the final output data.

The retrieval algorithm itself, however, is not developed using directly observed target variables. Sea-ice emissivity and its corresponding emission temperature are not available as observational datasets with sufficient spatial and temporal coverage for long-term data production. Instead, proxy target variables are constructed using physically based estimates of $\{\varepsilon, T_e\}$ derived from an established snow/sea-ice forward-modeling framework (Tonboe, 2010; Kang et al., 2021, 2023).

To ensure a physically consistent relationship between predictors and targets, TOA TBs are not taken directly from observations but are simulated using the Fast Radiative Transfer for TOVS (RTTOV; Saunders et al., 2018), with inputs of the modeled ε and T_e and collocated ECMWF Reanalysis v5 (ERA5) atmospheric temperature and humidity (T/q) profiles. This design preserves internal consistency between the predictor {TB} and target $\{\varepsilon, T_e\}$ variables, providing a robust basis for simulation-based training and verification of the retrieval algorithm. Accordingly, the upstream forward-model-generated $\{\varepsilon, T_e\}$ is addressed in the data section rather than in the algorithm-development section. The present study instead focuses on the

https://doi.org/10.5194/essd-2026-471
Preprint. Discussion started: 24 August 2026

development, validation, and application of the ML-based retrieval algorithm for the production of a consistent long-term dataset.

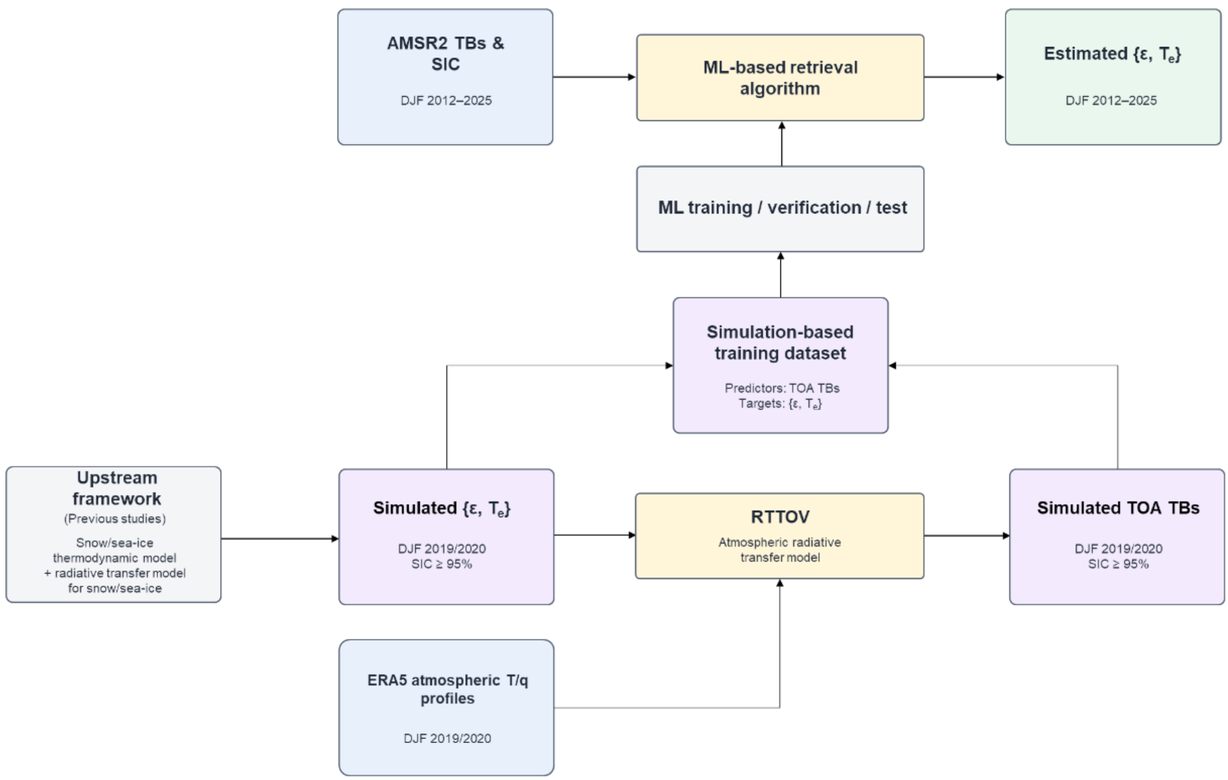

Figure 1. Schematic summary of the data flow in the retrieval framework.

2.2 Data sources

As indicated in Fig. 1, AMSR2-observed TBs and SIC are used directly to generate the final dataset. Reanalysis-based atmospheric T/q profiles, together with model-based ε and T_e, are used to simulate TOA TBs and thereby construct the training dataset for retrieval development. A climatological emissivity atlas and ground-based TB measurements provide a benchmark and field-based reference for dataset assessment, respectively, while sea-ice type supports complementary ice-type-classified analyses.

2.2.1 AMSR2 brightness temperature

AMSR2 is a multi-purpose passive microwave imaging radiometer aboard GCOM-W1, continuing the lineage of AMSR on ADEOS-2 and AMSR-E on Aqua. It is a conical-scanning sensor with a near-constant incidence angle of about 55° and provides 14 channels at seven central frequencies (6.925, 7.3, 10.65, 18.7, 23.8, 36.5, and 89.0 GHz) in both vertical (V) and horizontal (H) polarization, including atmospheric-window bands and a weak water-vapor absorption band at 23.8 GHz.

https://doi.org/10.5194/essd-2026-471
Preprint. Discussion started: 24 August 2026

AMSR2 offers near-daily global coverage with a swath width of about 1450 km; footprint size of about 5–62 km, and a typical noise-equivalent temperature difference (NEΔT) of 0.3–1.1 K (Table 1). In this study, AMSR2 Level-1R granule TBs (Maeda et al., 2016) are used as the observational input to the retrieval during boreal winter (December–January–February; DJF) for 2012–2025.

Table 1. Detailed characteristics of AMSR2

<table>
<tr><th>Channel
No.</th><th>Central frequency
(GHz)</th><th>Bandwidth
(MHz)</th><th>Polarization</th><th>NEΔT
(K)</th><th>Pixel size
(km × km)</th></tr>
<tr><td>1</td><td rowspan="2">6.925</td><td rowspan="4">350</td><td>V</td><td rowspan="4">0.3</td><td rowspan="12">10 × 10</td></tr>
<tr><td>2</td><td>H</td></tr>
<tr><td>3</td><td rowspan="2">7.3</td><td>V</td></tr>
<tr><td>4</td><td>H</td></tr>
<tr><td>5</td><td rowspan="2">10.65</td><td rowspan="2">100</td><td>V</td><td rowspan="8">0.6</td></tr>
<tr><td>6</td><td>H</td></tr>
<tr><td>7</td><td rowspan="2">18.7</td><td rowspan="2">200</td><td>V</td></tr>
<tr><td>8</td><td>H</td></tr>
<tr><td>9</td><td rowspan="2">23.8</td><td rowspan="2">400</td><td>V</td></tr>
<tr><td>10</td><td>H</td></tr>
<tr><td>11</td><td rowspan="2">36.5</td><td rowspan="2">1000</td><td>V</td></tr>
<tr><td>12</td><td>H</td></tr>
<tr><td>13</td><td rowspan="2">89.0</td><td rowspan="2">3000</td><td>V</td><td rowspan="2">1.1</td><td rowspan="2">5 × 5</td></tr>
<tr><td>14</td><td>H</td></tr>
</table>

2.2.2 OSI SAF sea-ice concentration and type

OSI SAF daily SIC is used to define the sea-ice analysis domain. SIC represents the fractional sea-ice cover within each grid cell, ranging from 0 for open water to 1 for compact sea ice. Because ERA5 also uses OSI SAF daily SIC to specify its sea-ice boundary condition (Lavergne et al., 2019) via the Operational Sea Surface Temperature and Sea Ice Analysis (OSTIA; Donlon et al., 2012), with the boundary updated daily, its use here helps maintain consistency with the other ERA5 variables used throughout the workflow. In this study, the SIC fields are used to apply concentration-based screening for delineating the Arctic sea-ice domain.

OSI SAF daily sea-ice type is used to classify sea ice as first-year ice (FYI) or multiyear ice (MYI). The classification is based on a Bayesian approach that combines information from passive microwave radiometers and active microwave scatterometers (Aaboe et al., 2021). The probability density functions (PDFs) for FYI and MYI are derived from representative sectors

https://doi.org/10.5194/essd-2026-471
Preprint. Discussion started: 24 August 2026

between Greenland and Canada for MYI, and the Kara Sea, Baffin Bay, Laptev Sea, and Barents Sea for FYI. The PDFs are updated using observations aggregated from the preceding 15 days to account for the drift and evolution of sea ice. In this study, the sea-ice type fields are used to assess whether the retrieved sea-ice surface emission parameters preserve the characteristic FYI–MYI contrasts.

2.2.3 Model-based sea-ice emissivity and emission temperature

Sea-ice surface emission parameters (ε, T_e) are generated using the forward-modeling framework that couples a snow/sea-ice thermodynamic model with a snow/sea-ice radiative transfer model (Kang et al., 2021; 2023). Briefly, the thermodynamic components solve a one-dimensional (1D) layered heat-budget/diffusion system along 2D Lagrangian ice trajectories, representing each column with multiple snow and ice layers of 1–3 cm with layer-specific thermal conductivities that vary with the evolving snow and sea-ice properties. At the upper boundary, the surface energy balance is diagnosed from reanalysis-based atmospheric forcing. The snowpack evolves prognostically; snowfall from reanalysis precipitation as a form of atmospheric forcing is added to the uppermost layer and converted to snow depth using a snow-density parameterization (Jordan et al., 1999). The snowpack subsequently evolves through metamorphism and compaction (Kojima, 1967; Anderson, 1976; Jordan, 1991), together with parameterized grain-size evolution (Marbouty, 1980). When negative freeboard occurs, submerged snow is allowed to refreeze as saline snow ice (Fichefet and Morales Maqueda, 1999). At the lower boundary, the sea-ice/ocean interface is constrained by a prescribed ocean temperature of −1.8 ℃, and basal sea-ice growth or melt is determined from the balance between conductive heat flux through the sea ice and oceanic heat flux. To better constrain the thermal structure, satellite-retrieved temperatures at the uppermost snow and sea-ice layers, derived from infrared and microwave radiometers, are respectively nudged into the model.

Previous evaluations assessed the key simulated variables against literature-based characteristics and observation-based measurements (Kang et al., 2021). The model reproduces the large-scale contrast between thicker snow cover over MYI sectors and thinner snow cover over FYI sectors. Regional-mean snow depths of around 10–30 cm and winter snow-accumulation rates of around 2 cm month^{-1} are broadly consistent with snow climatologies and other snow-model estimates. Simulated snow densities of approximately 300–400 kg m^{-3} also fall within the ranges reported by Arctic field campaigns and other snow-model estimates. Against Operation IceBridge (OIB) aircraft measurements collected along 24 flight tracks during 2013–2015, the simulated snow depth yielded a linear correlation coefficient (r) of 0.73, a mean deviation (b) of about 6 cm, and a standard deviation (σ) of about 6 cm (Kang et al., 2021, Fig. 12). Corresponding evaluations yielded $r = 0.76$, $b \approx 3$ cm, and $\sigma \approx 12$ cm for total freeboard against OIB measurements along the same flight tracks (Kang et al., 2021, Fig. 13), and $r = 0.59$, $b \approx -3$ cm, and $\sigma \approx 5$ cm for ice freeboard against CryoSat-2 satellite estimates across the Arctic Basin during 2013–2015 (Kang et al., 2021, Fig. 16). Comparisons with ice-mass-balance buoy measurements further showed reasonable agreement for the simulated snow- and ice-layer temperatures, with $r \approx 0.8$–0.9, $|b| \leq 1$ K, and $\sigma \approx 2$ K (Kang et al., 2021, Fig. 17). Together, these comparisons indicate that the simulated snow/sea-ice states reproduce the observed spatial and seasonal characteristics of Arctic winter sea ice with reasonable fidelity and remain within observationally plausible ranges.

https://doi.org/10.5194/essd-2026-471
Preprint. Discussion started: 24 August 2026

The resulting layered snow/ice states are then passed to the snow/sea-ice radiative transfer model to diagnose ε and T_e at AMSR2 central frequencies. Because AMSR2 is a conically scanning sensor with a near-constant incidence angle, viewing-geometry variability is minimal. In this study, the resulting ε and T_e fields are produced every 6 h on a 25 km × 25 km equal-area grid over the Arctic Ocean north of 70°N for winter 2019/2020 (DJF), under compact sea-ice conditions (SIC ≥ 95%). These fields are used in two ways within the retrieval framework. First, they serve as the target variables for training the ML-based retrieval. Second, they are used as lower boundary conditions in RTTOV forward simulations to construct simulation-based TB vs. {ε, T_e} pairs and to support simulation-based training and verification of the retrieval algorithm. In Kang et al. (2023), the simulated TBs reproduced the observed AMSR2 TBs well, with high correlations, small biases, and channel-wise spread generally within about 3 K. The resulting ε and T_e fields were successfully applied as lower boundary conditions in standalone one-dimensional variational (1D-Var) experiments, enabling the use of surface-sensitive temperature sounding channels and improving lower-tropospheric temperature retrievals. This supports their suitability as training targets for the ML-based retrieval.

2.2.4 ERA5 atmospheric temperature and moisture profiles

ERA5 is the fifth-generation reanalysis of ECMWF, produced with the Integrated Forecasting System (IFS; cycle 41r2) using an atmospheric hybrid 4D-Var and land data assimilation systems (Hersbach et al., 2020; Bell et al., 2021). It provides hourly global atmospheric and surface fields on a 0.25° × 0.25° regular latitude–longitude grid with 31 pressure-levels up to 1 hPa and a single surface level. In this study, hourly ERA5 atmospheric T/q profiles are used as essential inputs to RTTOV in two parts of the retrieval framework. First, ERA5 T/q profiles for winter 2019/2020 (DJF) are combined with the model-based sea-ice surface emission parameters, described in Section 2.2.3, to generate AMSR2 TOA TBs and construct the simulation-based training dataset for retrieval development. Second, over the full AMSR2 observational period (Section 2.2.1), the retrieved surface parameters are combined with ERA5 T/q profiles in RTTOV to simulate TOA TBs for comparison with AMSR2 observations.

For a cloud-sensitivity test during winter 2019/2020 (DJF), ERA5 cloud-related variables, including hydrometeor and cloud fraction profiles, are additionally used in RTTOV-SCATT (RTTOV including scattering; Bauer et al., 2006) to estimate the magnitude of cloudy-sky effects on AMSR2 TBs. This test is intended to support the clear-sky approximation adopted in the main retrieval-development and application procedures. In addition, ERA5 atmospheric T/q profiles together with skin temperatures (T_s) are used in the top-down emissivity retrieval that serves as external benchmark for evaluating the final product.

2.2.5 TELSEM2 climatological sea-ice emissivity atlas

The Tool to Estimate Land Surface Emissivity from Microwave to Submillimeter Waves, version 2 (TELSEM2; Wang et al., 2017), is a monthly surface-emissivity atlas that extends the original TELSEM (Aires et al., 2011) to include sea-ice emissivity, and is widely used as a practical first-guess emissivity in community fast radiative transfer models such as RTTOV. In

https://doi.org/10.5194/essd-2026-471
Preprint. Discussion started: 24 August 2026

TELSEM2, anchor emissivities are obtained through clear-sky radiative transfer inversion (under skin-emission and specular-reflection assumptions) by combining window-channel observations with reanalysis-based atmospheric and surface constraints, that is, a top-down inversion approach. The resulting emissivities are aggregated by month and grouped into sea-ice classes, then averaged and parameterized to construct a gridded atlas as a function of frequency and viewing geometry. In this study, TELSEM2 serves as an external benchmark for evaluating the final product.

2.2.6 UoM SBR brightness temperature

The University of Manitoba Surface Based Radiometer (UoM SBR) is a ground-based microwave radiometer deployed during Legs 1–5 of the MOSAiC expedition (Rostosky et al., 2023). The quality-controlled product provides calibrated TBs at 19, 37, and 89 GHz in V/H-pols, at incidence angles of 45°, 50°, and 55° with a temporal resolution of 1-min after the removal of unstable periods, calibration events, anomalous scans, and outliers. For Legs 2 and 3, a 30-min moving-average is additionally applied across the channels to remove periodic fluctuations and to facilitate comparison across frequencies. As documented by Rostosky et al. (2023), the 37 GHz channel was unstable during substantial portions of the campaign, leaving only a limited number of usable periods.

The UoM SBR observations provide rare in situ measurements at frequencies close to those of AMSR2 and serve as an independent field-based reference for assessing the radiometric consistency of the retrieved sea-ice surface emission parameters. The usable overlap with our retrieval period was limited to MOSAiC Leg 2 from December 2019 to February 2020, during which the MOSAiC site was located on a second-year ice-dominated floe (Nicolaus et al., 2022). We used the UoM SBR TBs at 19 and 37 GHz V/H-pols at an incidence angle of 55°, as the closest available counterparts to the AMSR2 channels used in this study. The 1-min UoM SBR measurements were collocated with the nearest AMSR2 grid cells. The mean temporal separations were less than 1 min, and the mean spatial separations were about 4–6 km. The resulting collocated samples are summarized in Table 2.

Table 2. Summary of quality-controlled UoM SBR measurements during MOSAiC Leg 2.

Central frequency (GHz)	Bandwidth (GHz)	Polarization	Available dates	Days	Records (1-min res.)	Collocated samples	Mean |Δt| (min)	Mean Δx (km)
19 GHz	1	V/H	23–26 Dec 2019 16–18 Jan 2020 21–24 Jan 2020 7–10 Feb 2020 12–15 Feb 2020 17–18 Feb 2020 22 Feb 2020	22	19,267	90	0.41	6.1
37 GHz	4	V/H	25 Dec 2019 11–12 Feb 2020 17–20 Feb 2020	7	4,568	24	0.34	4.4

https://doi.org/10.5194/essd-2026-471
Preprint. Discussion started: 24 August 2026

3 Retrieval Methodology

This section presents the retrieval methodology, covering the theoretical basis for the radiative transfer approximation (Section 3.1), the algorithm development through inverse formulation, simulation-based training-data construction, and artificial neural network (ANN) design (Section 3.2), and the workflow for generating the final dataset (Section 3.3).

3.1 Theoretical basis for radiative transfer approximation in window channels

The retrieval algorithm developed in this study is based on the premise that, under winter Arctic cold and dry conditions, TOA TBs in low-frequency microwave window channels are mainly controlled by surface emission, with only weak and slowly varying atmospheric contributions. This allows the inverse mapping from TOA TBs to surface emission parameters, ε and T_e, to be treated as a sufficiently constrained problem under the winter Arctic conditions.

The TOA TB can be expressed using a plane-parallel radiative transfer formulation as

$$TB_i = \Upsilon_i \left[\varepsilon_i T_{e,i} + \left(1-\varepsilon_i\right) TB_i^{\downarrow} \right] + TB_i^{\uparrow} \tag{1}$$

where Υ denotes the total atmospheric transmittance, and $TB^{\downarrow}$ and $TB^{\uparrow}$ represent the down-welling and upwelling atmospheric emission TBs, respectively. Here, the subscript i denotes the channel index. For the window-channel frequencies considered here (18.7, 23.8, and 36.5 GHz), atmospheric absorption and scattering are weak, particularly under cold and dry Arctic winter conditions. Radiative transfer simulations using RTTOV with ERA5 atmospheric T/q profiles over the Arctic Ocean during DJF 2019/2020 show that transmittances at these frequencies remain high ($\Upsilon > 0.9$), while atmospheric emission contributes only a small fraction of the total signal (typically 7–22 K, corresponding to less than 10% of TOA TB; Fig. 2). Moreover, the variability of these atmospheric terms is found to be small, with channel-dependent standard deviations of $\boldsymbol{O}(10^{-3})$ for Υ and less than a few Kelvin for $TB^{\downarrow}$ and $TB^{\uparrow}$ under the Arctic winter conditions. Even at 23 GHz, where weak water-vapor absorption is present, the variability remains below approximately 1% of the total signal (Kang et al., 2026).

https://doi.org/10.5194/essd-2026-471
Preprint. Discussion started: 24 August 2026

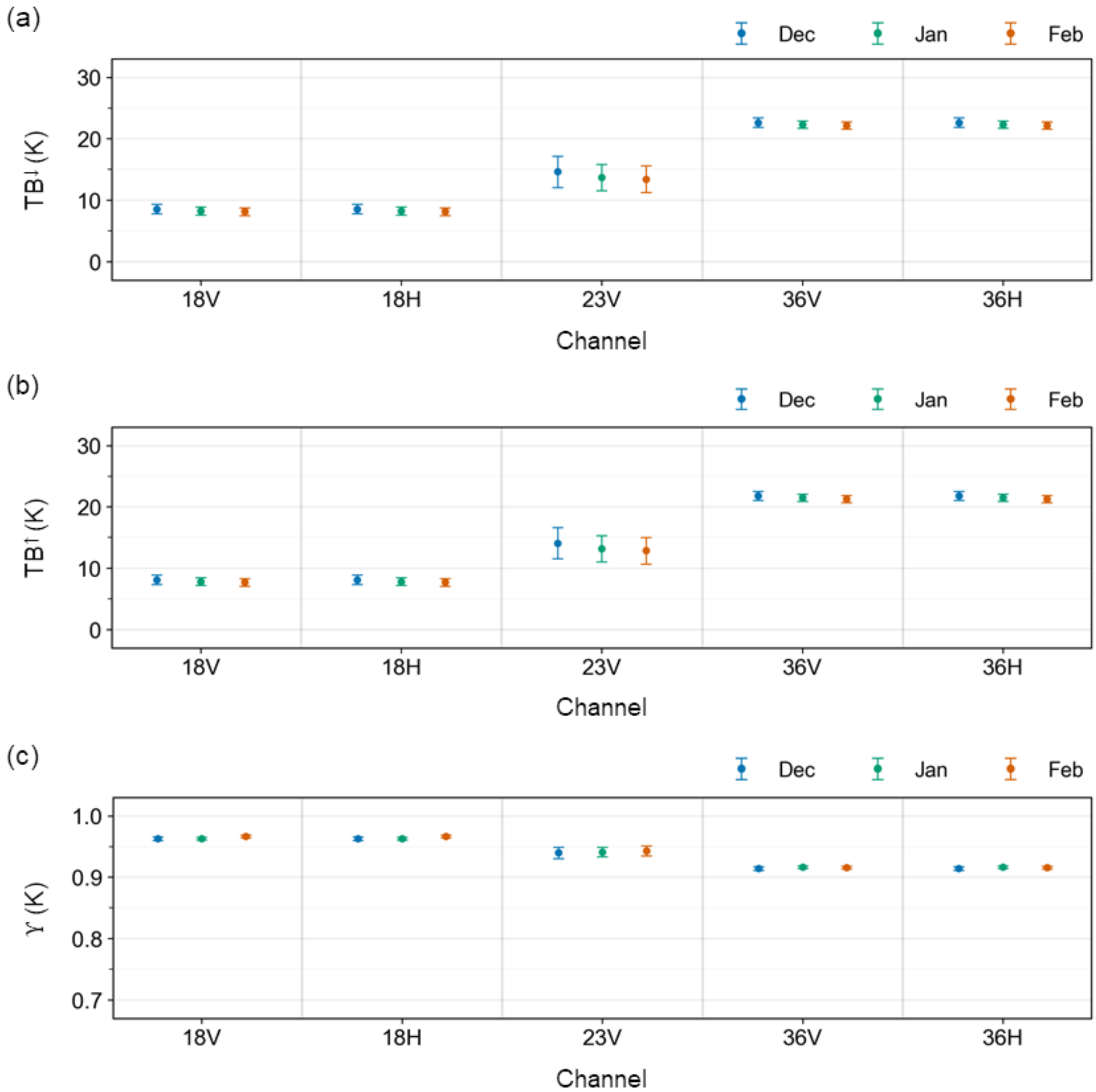

Figure 2. Atmospheric terms for the five channels (18V/H, 23V, 36V/H) over winter Arctic: DJF 2019/2020 monthly means ±1 s.d. of (a) total atmospheric transmittance (ϒ) and (b)–(c) upwelling and downwelling atmospheric emission ($TB^{\uparrow}$, $TB^{\downarrow}$).

Given these characteristics, the radiative transfer equation can be approximated by treating the atmospheric terms (ϒ, $TB^{\downarrow}$ and $TB^{\uparrow}$) as channel-dependent constants, yielding a simplified linear form:

$$TB_{i} = a_{i}\left(\varepsilon_{i} T_{e,i}\right) + b_{i}\left(\varepsilon_{i}\right) + c_{i} \tag{2}$$

where a = ϒ, b = − ϒ $TB^{\downarrow}$, and c = ϒ $TB^{\downarrow}$ + $TB^{\uparrow}$. Under this approximation, the first term is dominant, while the second and third terms are much smaller. Accordingly, TOA TB is governed mainly by the coupled surface term $\varepsilon \cdot T_e$, while atmospheric

https://doi.org/10.5194/essd-2026-471
Preprint. Discussion started: 24 August 2026

effects act as secondary offsets with limited variability. This simplifies the inverse problem and provides the theoretical basis for relating TOA TBs directly to surface parameters without explicitly resolving atmospheric components.

Because this argument is derived under clear-sky assumptions, it is necessary to assess the potential impact of clouds. A previous study has shown that cloud effects in low-frequency microwave channels are generally weak at high latitude cold regions (Bormann, 2022). Consistent with this, sensitivity tests using cloudy-sky radiative transfer simulations with prescribed hydrometeor profiles indicate that the difference between clear-sky and cloudy-sky TOA TBs is uniformly small (typically less than 1 K across the channels at the frequencies considered here). These differences are negligible compared with the surface-driven signal and its variability, thereby supporting the use of a clear-sky approximation without explicit cloud screening in the construction of the retrieval framework.

The physical meaning of the surface parameters can be understood by considering microwave radiation emerging from a vertically inhomogeneous snow and sea-ice medium. In the Rayleigh–Jeans limit, the surface emission (TB^{sfc}) can be expressed as a depth-integrated contribution,

$$TB_{\mathrm{i}}^{\mathrm{sfc}} = \int_0^{z_b} W_{\mathrm{i}}(z)\, T(z)\, dz \tag{3}$$

where T(z) is the temperature profile within the snow/sea-ice column, W(z) is a channel-dependent weighting function describing the relative contribution from depth z, and z_b is the ice thickness. This formulation can be approximated by a homogeneous-boundary representation (Phalippou, 1992), in which

$$TB_{\mathrm{i}}^{\mathrm{sfc}} = \varepsilon_{\mathrm{i}} T_{\mathrm{e,i}} \tag{4}$$

where T_e represents a weighting-function-weighted temperature of the contributing layer, and ε summarizes the net radiative coupling between T_e and TB^{sfc}, as given by

$$T_{e,i} \equiv \frac{\int_0^{z_b} W_{\mathrm{i}}(z)\, T(z)\, dz}{\int_0^{z_b} W_{\mathrm{i}}(z)\, dz} \tag{5}$$

and

$$\varepsilon_{\mathrm{i}} \equiv \int_0^{z_b} W_{\mathrm{i}}(z)\, dz \tag{6}$$

The feasibility of retrieving these parameters from multi-channel observations arises from the frequency dependence of the weighting functions. At the frequencies considered here (18.7, 23.8, and 36.5 GHz), the overlying dry snow is nearly

https://doi.org/10.5194/essd-2026-471
Preprint. Discussion started: 24 August 2026

transparent, and the observed signal is therefore controlled mainly by the upper sea ice (Lee et al., 2017; Baek et al., 2023). The 18.7 GHz channel penetrates more deeply into the sea ice than the 36.5 GHz channel, but all channels still share a substantial overlap in their contributing depth ranges. This overlap allows T_e to be constrained through cross-channel coherence in observed TBs. Once T_e is constrained, the relationship between TB^{sfc} and ε becomes better conditioned, enabling a stable separation of ε and T_e.

Although the retrieval framework relies on the relative transparency of dry snow at these frequencies, the model-based training targets are nevertheless generated using a snow/sea-ice configuration. It is therefore important to assess whether plausible uncertainties in the prescribed snowpack could substantially modify the radiative-boundary conditions used for retrieval training. To examine this possibility, we use the emissivity as a diagnostic and conduct a one-at-a-time sensitivity test by independently perturbing snow density, temperature, and depth around a representative Arctic winter snowpack configuration (Fig. S1). The resulting emissivity changes are small across the low-frequency channels considered here, with maximum absolute changes below approximately 6×10^{-3}, corresponding to less than 1% of typical sea-ice emissivity. This weak sensitivity is consistent with previous low-frequency microwave studies indicating that, under cold and dry Arctic winter conditions, surface emission is governed mainly by the underlying sea ice rather than by the overlying snowpack (Schanda et al., 1983; Mathew et al., 2009; Lee et al., 2017; Baek et al., 2023). Thus, as indicated by the weak emissivity response, the snowpack uncertainty is unlikely to exert a first-order influence on the model-based sea-ice radiative-boundary parameters subsequently used as retrieval-training targets.

Together, these considerations demonstrate that, for the channel configuration considered here under winter Arctic conditions, TOA TBs provide a physically robust and sufficiently constrained basis for retrieving penetration-aware, channel-dependent sea-ice emission parameters. This establishes the foundation for the inverse mapping developed in the following section.

3.2 Algorithm development

Based on the theoretical framework established in Section 3.1, the retrieval of surface emission parameters can be formulated as an inverse problem that maps multi-channel TOA TBs to channel-dependent ε and T_e. In this section, we first define this inverse relationship and the associated predictor–target structure (Section 3.2.1), then describe the construction of simulation-based training dataset (Section 3.2.2), and finally present the ANN retrieval algorithm used to learn the mapping (Section 3.2.3).

3.2.1 Relating TOA TBs to ε and T_e

The retrieval problem in this study can be formulated as a multivariate nonlinear mapping from TOA TBs to surface emission parameters. Specifically, we define the inverse problem as

$$X = \{TB_i\}_{i=1}^{N} \mid \;\rightarrow\; \mid Y = \{\varepsilon_{ch}, T_{e,ch}\}_{ch \in C_{out}} \tag{7}$$

https://doi.org/10.5194/essd-2026-471
Preprint. Discussion started: 24 August 2026

where X denotes the predictor vector of TOA TBs across selected channels, and Y represents the target vector of channel-wise ε and T_e. Here, N is the number of input channels, while ch and C_{out} denote the output-channel label and the set of output channels, respectively.

A key design choice in this study is the use of TOA TBs directly as predictors, rather than attempting to retrieve or estimate surface-level TB prior to inversion. This choice is justified in Section 3.1, which demonstrates that, for low-frequency microwave window channels under winter Arctic conditions, atmospheric effects are small and weakly variable, and can be approximated as channel-dependent constants. As a result, TOA TBs retain a near-linear relationship with the surface emission term ε·Te, allowing the inverse mapping to be constructed directly in observation space without explicit atmospheric correction.

The predictor vector is constructed using channels within the low-frequency microwave window region, specifically 18.7, 23.8, and 36.5 GHz, which have been widely used in passive-microwave sea-ice applications. Because these channels provide complementary vertical sensitivity, their combined use introduces cross-channel coherence that is important for constraining T_e and, subsequently, ε, as discussed in Section 3.1.

The input vector is defined using five TOA TBs.

$$X = \{TB_{18V}, TB_{18H}, TB_{23V}, TB_{36V}, TB_{36H}\} \tag{8}$$

while the output vector is defined as

$$Y = \{\varepsilon_{ch}, Te_{ch}\}_{ch \in (18V,\ 18H,\ 23V,\ 23H,\ 36V,\ 36H)} \tag{9}$$

An important aspect of this configuration is the asymmetric treatment of the 23 GHz H-pol (23H) channel. While 23H is included in the output targets, it is excluded from the input predictors. This design is motivated by long-term data continuity and algorithm robustness. Specifically, the 23H channel is not consistently available in earlier satellite missions, including the Special Sensor Microwave/Imager (SSM/I) and the Special Sensor Microwave Imager/Sounder (SSMIS), and excluding it from the input ensures that the retrieval framework can be applied across multi-decadal climate data records from SMMR–SSM/I–SSMIS–AMSR series (Fennig et al., 2020; Kummerow et al., 2022). At the same time, including 23H in the output provides two benefits. First, it enables reconstruction of 23H surface parameters for historical periods when direct observations are not available. Second, for sensors such as AMSR2 that observe 23H, it allows an independent consistency check by comparing the forward-simulated 23H TB from the retrieved surface parameters with the actual observation, since the retrieval itself is not directly constrained by 23H input.

https://doi.org/10.5194/essd-2026-471
Preprint. Discussion started: 24 August 2026

Through this formulation, the inverse problem is defined in a physically consistent and observation-driven manner, enabling the subsequent development of a data-driven retrieval algorithm that exploits the relationship between TOA TBs and surface emission properties.

3.2.2 Construction of simulation-based training dataset

To realize the inverse mapping defined in Section 3.2.1, a dataset of physically consistent predictor–target pairs is required, linking TOA TBs to the corresponding surface emission parameters. Such a target dataset is not directly available from observations, because ε and T_e cannot be independently measured at the spatial and temporal scales of interest. We therefore construct a simulation-based dataset using forward radiative transfer calculations, ensuring consistency between predictors and targets. For each sample, model-based {ε, T_e}, described in Section 2.2.3, together with ERA5 atmospheric T/q profiles are used in RTTOV to simulate TOA TBs for the selected channels as predictors, X, while the corresponding channel-wise {ε, T_e} are retained as targets, Y, forming predictor–target pairs (X, Y).

All simulations are performed under clear-sky conditions, consistent with the approximation established in Section 3.1. Accordingly, no cloud screening or hydrometeor profiles are included in the dataset construction. The training dataset is generated over Arctic winter conditions during DJF 2019/2020 and is restricted to the Arctic Ocean north of 70°N with SIC ≥ 95%. The 95% threshold accounts for the intrinsic uncertainty of SIC retrievals near their upper bound because tie-point-based algorithms scatter around 100% by 1.9–5.0%, depending on the algorithm, even over a complete ice cover (Ivanova et al., 2015; Kern et al., 2019). A 5% margin below 100% was therefore adopted so as to encompass the largest spread. This domain selection thereby ensures stable ice-covered conditions with minimal open-water contamination.

The resulting dataset provides approximately one million physically consistent samples spanning realistic atmospheric and surface variability, and thus forms the basis for supervised learning of the inverse mapping defined in Section 3.2.1. Each sample consists of five simulated TOA TBs at 18V/H, 23V, and 36V/H as predictors, together with nine targets comprising six ε at 18V/H, 23V/H, and 36V/H and three T_e at 18, 23, and 36 GHz. The targets include three rather than six T_e because Kang et al. (2025) showed that T_e of the two polarizations at a given frequency are almost identical. A single T_e is therefore assigned per frequency. The complete set of pairs is archived together with the retrieval product (Kang, 2026) and its detailed structure is described in Section 7.

3.2.3 ANN retrieval algorithm

Using the simulation-derived predictor–target pairs, the retrieval operator R is learned to map the TOA TB vector X to the target vector Y composed of ε and T_e:

$$R : X \rightarrow Y \tag{10}$$

https://doi.org/10.5194/essd-2026-471
Preprint. Discussion started: 24 August 2026

Because ε and T_e represent physically distinct quantities with different statistical characteristics, we train two independent ANN with identical architectures: one for emissivity and one for emission temperature. This separation improves optimization stability and allows each network to specialize in learning the distribution of its respective target variable.

The full dataset, on $\boldsymbol{O}(10^6)$ samples, is randomly divided into three mutually exclusive subsets: 60% for learning, 20% for validation, and 20% for testing. Prior to training, both predictors and targets are normalized to improve convergence during gradient-based optimization. The network architecture and hyperparameters are selected using AutoKeras, a Keras-based AutoML library (Jin et al., 2023), which explores candidate configurations using the learning and validation subsets. Early stopping based on validation loss is applied to prevent overfitting.

Each target-specific ANN is denoted by f(X, α), where X is the input vector and α represents the learned weights and biases. The selected ANN architecture is a fully connected multilayer perceptron consisting of two hidden layers with 2^8 and 2^9 neurons, respectively, using rectified linear unit (ReLU) activation functions. A dropout layer with a rate of 0.5 is applied after the second hidden layer to improve generalization. The output layer is linear, producing channel-wise estimates of the target variables.

Denoting ReLU activation by $\phi(\cdot)$ and the layer coefficient sets by $\alpha=\{W_i, b_i\}$ for i=1,2,3, the network can be expressed as

$$f(X,\alpha) = W_3\,\phi\big(W_2\,\phi(W_1 X + b_1) + b_2\big) + b_3 \tag{11}$$

The two networks share the same architecture and training protocol but are trained independently, yielding target-specific coefficient sets. The final retrieval operator is thus

$$R(X,\Theta) = \{f(X,\alpha_\varepsilon),\, f(X,\alpha_{Te})\} = Y \tag{12}$$

with $\Theta = \{\alpha_\varepsilon, \alpha_{Te}\}$ denoting the two independently learned coefficient sets. The final retrieval algorithm provides channel-wise estimates of ε and T_e from TOA TBs, yielding a flexible data-driven representation of the inverse mapping while preserving the physically motivated structure established in the preceding sections.

3.3 Production workflow

The final dataset is produced by applying the retrieval algorithm developed in Section 3.2 to AMSR2 observations. Specifically, the trained ANN is applied to AMSR2 multi-channel TBs to generate a consistent record of sea-ice surface emission parameters. The input data consist of AMSR2 TBs at the selected window channels, acquired over the Arctic Ocean north of 70°N during boreal winter (DJF) for the period 2012–2025. To ensure consistency with the training conditions, retrievals are restricted to compact sea-ice regions using SIC fields. Only grids with SIC ≥ 95% are retained, thereby minimizing contamination from open-water signals and marginal ice zones. As an additional precaution, a TB-based weather-effect filter is applied to remove

https://doi.org/10.5194/essd-2026-471
Preprint. Discussion started: 24 August 2026

spurious observations affected by atmospheric disturbances that can mimic sea-ice signals, following the NASA Team filter for AMSR2 in the Northern Hemisphere (Meier et al., 2024), based on the long-established approach of Gloersen and Cavalieri (1986). In principle, however, proper SIC ≥ 95% screening should leave no additional observations to be removed by the weather filter.

The screened TOA TB vectors are then used as inputs to the retrieval operator R, which estimates channel-wise ε and T_e. The overall workflow, from input observations, through screening, to retrieval, is summarized in Fig. 3. The resulting dataset provides a temporally consistent winter record of surface emission parameters, which is evaluated against various independent references in the following section.

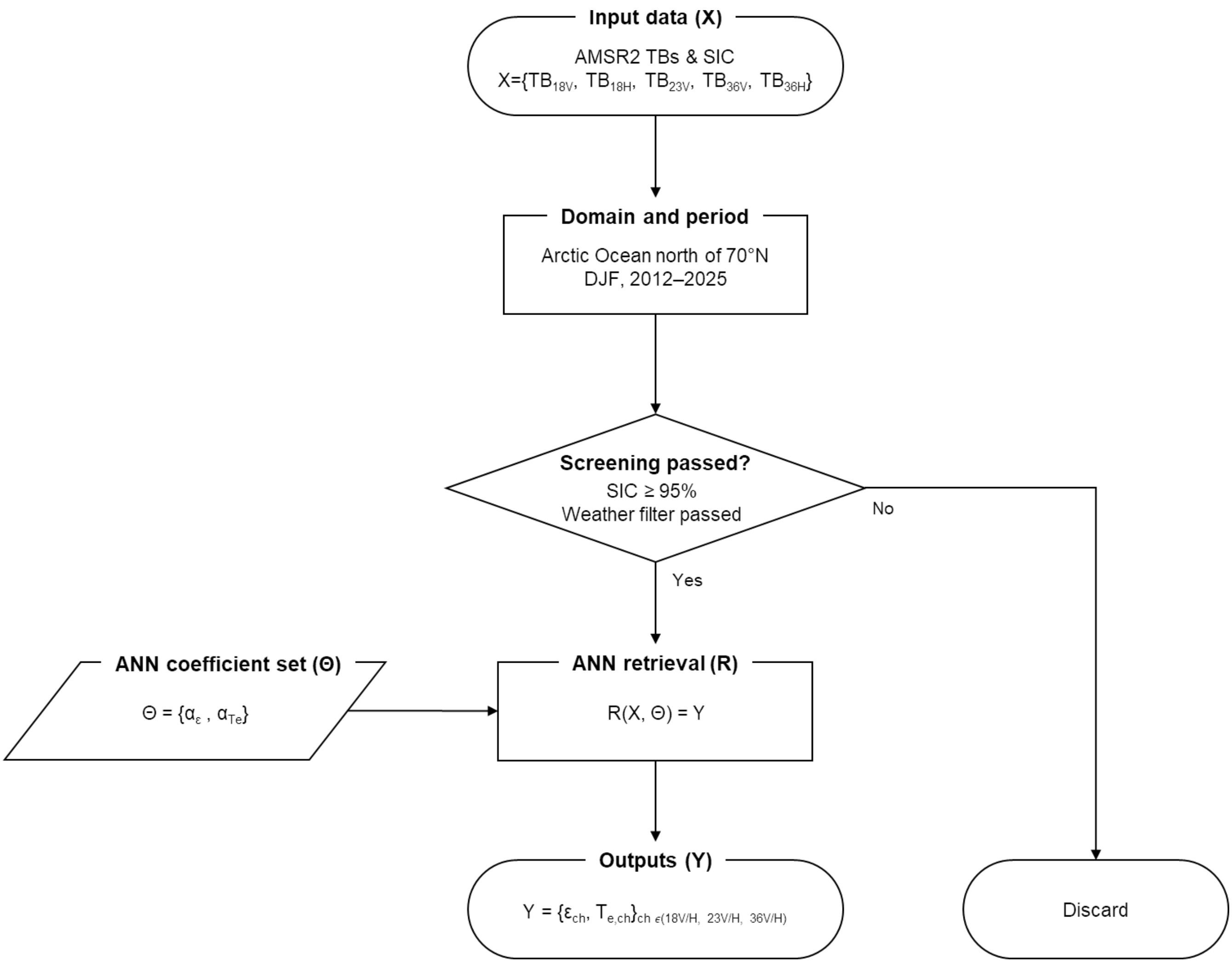

Figure 3. Schematic production workflow.

https://doi.org/10.5194/essd-2026-471
Preprint. Discussion started: 24 August 2026

4 Evaluation of retrieval performance and radiative consistency

In this section, we first verify retrieval skill and generalization ability using the validation and independent test subsets (Section 4.1). We then evaluate observation-space performance by comparing forward-simulated TOA TBs with AMSR2 winter observations (DJF 2012/2013–2024/2025), using deviation statistics and temporal stability, relevant to operational applications (Section 4.2). All analyses are restricted to the Arctic Ocean north of 70°N with SIC ≥ 95%.

4.1 Evaluation against simulation-based reference data

We assess retrieval skill against the reference targets of validation and test subsets for channel-wise ε and T_e, as well as their coupled term ($\varepsilon \cdot T_e$) at AMSR2 18V/H, 23V/H, and 36V/H channels. Accuracy is quantified using the linear correlation coefficient (r), systematic error (bias; b), and random error (σ). Figures 4–5 show retrieved-versus-reference scatterplots of ε, T_e and $\varepsilon \cdot T_e$, with accompanying error histograms for the validation subset, and Table 3 summarizes the statistics. To assess generalization, equivalent scatterplots for the test subset are provided in the Supplementary Material (Figs. S2–S3) and the corresponding statistics are listed in parentheses in Table 3.

Retrieved ε closely follows the 1:1 relationship with small dispersion across all channels (Fig. 4a–f) and reproduces the frequency- and polarization-dependent bimodal clustering associated with sea-ice type, including MYI and FYI. Consistently high correlations ($r > 0.99$), near-zero biases ($\boldsymbol{O}(10^{-4})$), and small error spread ($\sigma \approx 0.003$ to 0.005) confirm these visual agreements (Table 3). Retrieved T_e exhibits broader scatter than emissivity, but remains well aligned with the 1:1 line (Fig. 4g–i). Skill remain high correlations ($r \approx 0.94$ to 0.97) with small biases ($\boldsymbol{O}(10^{-2})$) and sub-kelvin error spread ($\sigma \approx 0.80$ to 0.94 K; Table 3). Unlike ε, T_e shows a unimodal distribution, as expected for a thermodynamic state variable. Although 18 GHz channels penetrate deeper (and thus warmer) layers under $\partial T/\partial z > 0$, yielding slightly higher T_e than 36 GHz channels, substantial overlap among weighting functions keeps T_e highly correlated across frequencies (Tonboe et al., 2011). Both error histograms are centered near zero and are approximately symmetric, indicating predominantly random residuals.

https://doi.org/10.5194/essd-2026-471
Preprint. Discussion started: 24 August 2026

Open Access Earth System Science Data Discussions

Table 3. Retrieval verification statistics for emissivity (ε), emission temperature (T_e), and surface emission ($\varepsilon \cdot T_e$) at six target channels (18V/H, 23V/H, 36V/H), correlation (r), mean error (b; retrieved − reference), and error spread (σ), for the validation subset. Corresponding values for the test subset are shown in parentheses.

	Central frequency (GHz)	**r**	**b**	**σ**
ε_V	18.7	0.99 (0.99)	0.0002 (0.0002)	0.0035 (0.0035)
	23.8	0.99 (0.99)	0.0000 (0.0000)	0.0039 (0.0039)
	36.5	0.99 (0.99)	0.0002 (0.0002)	0.0045 (0.0045)
ε_H	18.7	0.99 (0.99)	−0.0001 (−0.0001)	0.0034 (0.0034)
	23.8	0.99 (0.99)	0.0000 (0.0000)	0.0038 (0.0038)
	36.5	0.99 (0.99)	0.0004 (0.0004)	0.0043 (0.0043)
T_e (K)	18.7	0.97 (0.97)	0.02 (0.02)	0.80 (0.80)
	23.8	0.96 (0.96)	0.02 (0.02)	0.83 (0.83)
	36.5	0.94 (0.94)	0.01 (0.01)	0.94 (0.94)
$\varepsilon_V \cdot T_e$ (K)	18.7	0.99 (0.99)	0.08 (0.08)	0.38 (0.38)
	23.8	0.99 (0.99)	0.03 (0.03)	0.47 (0.47)
	36.5	0.99 (0.99)	0.08 (0.08)	0.59 (0.59)
$\varepsilon_H \cdot T_e$ (K)	18.7	0.99 (0.99)	−0.01 (−0.01)	0.46 (0.46)
	23.8	0.99 (0.99)	0.04 (0.03)	0.52 (0.52)
	36.5	0.99 (0.99)	0.11 (0.11)	0.60 (0.60)

https://doi.org/10.5194/essd-2026-471
Preprint. Discussion started: 24 August 2026

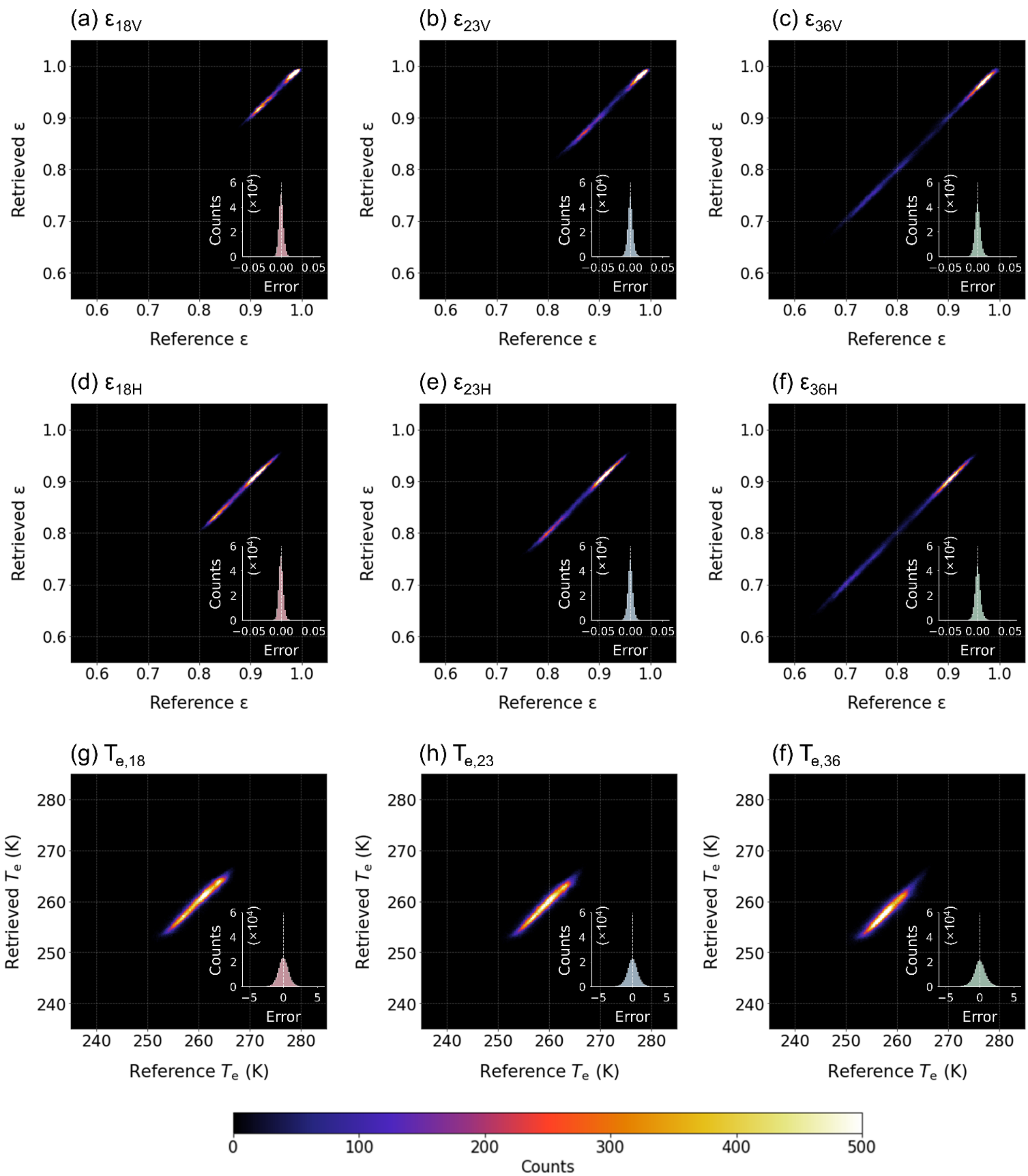

Figure 4. Scatterplots of retrieved versus reference channel-wise (a–f) emissivity (ε) and (g–i) emission temperature (T_e) for validation subset, with error histograms (retrieved – reference).

https://doi.org/10.5194/essd-2026-471
Preprint. Discussion started: 24 August 2026

The surface-emission term $\varepsilon \cdot T_e$, which primarily controls TOA TB in the radiative transfer equation (Eq. 2), matches the reference almost linearly across all channels (Fig. 5), yielding $r > 0.99$, $|b| < 0.1$ K, and $\sigma \approx 0.38$ to 0.60 K (Table 3). The bimodal structure associated with FYI-MYI contrasts is retained, indicating that the emissivity-driven contrast is preserved in the surface emission term. The corresponding error histograms are close to symmetric, indicating that the remaining errors are predominantly random.

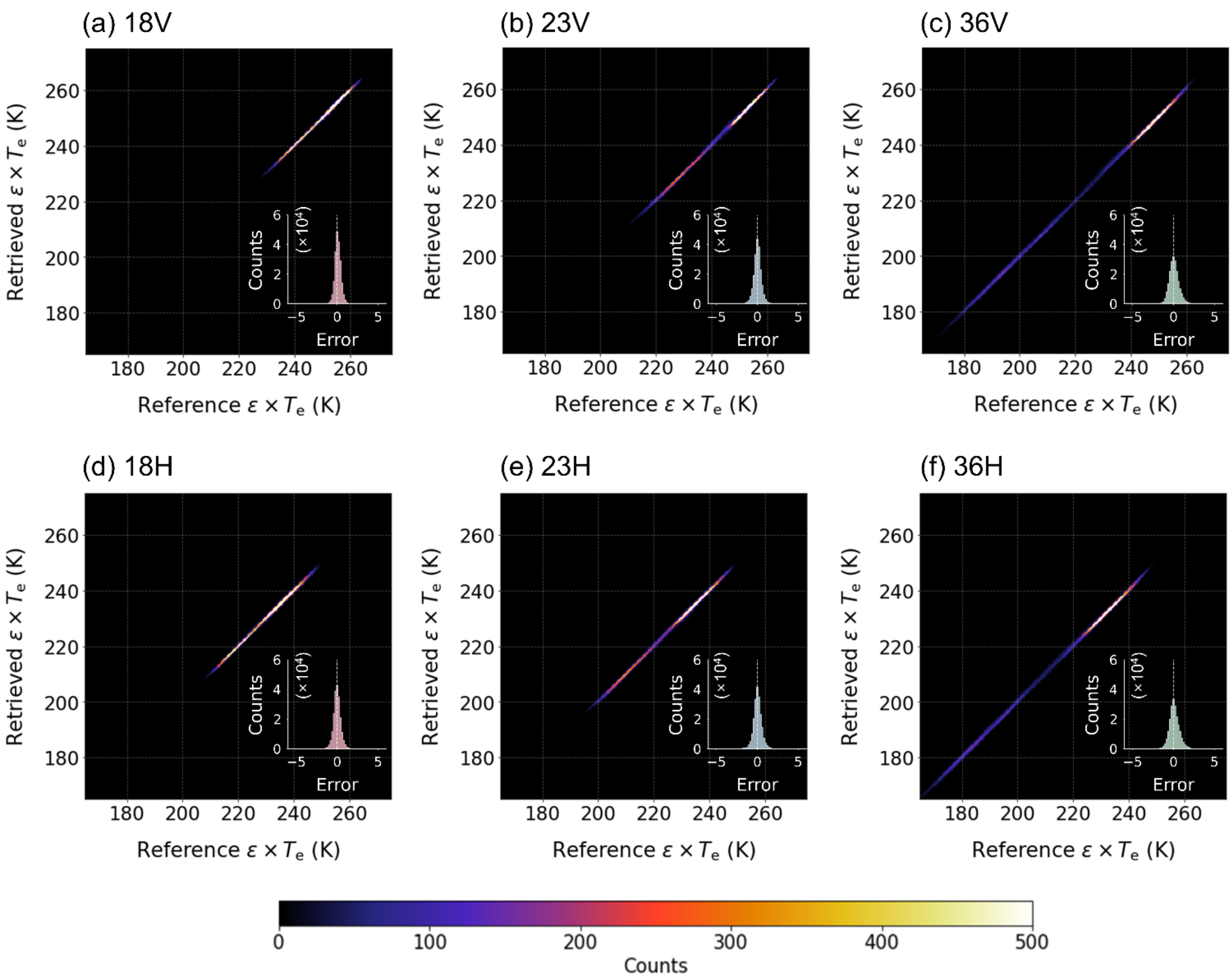

Figure 5. Scatterplots of retrieved versus reference channel-wise surface-emission ($\varepsilon \cdot T_e$) for validation subset, with retrieval-error histograms (retrieved – reference).

It is important to note that ε and T_e are retrieved using two independently trained networks, without imposing any explicit constraint on their coupled product (i.e., $\varepsilon \cdot T_e$). Despite this independence, the reconstructed $\varepsilon \cdot T_e$ shows excellent agreement

https://doi.org/10.5194/essd-2026-471
Preprint. Discussion started: 24 August 2026

with the references. This result is particularly significant because, in the radiative transfer framework, $\varepsilon \cdot T_e$ represents the effective surface boundary condition governing the surface-emitted signal. If the networks have been trained jointly on $\varepsilon \cdot T_e$, such agreement could be attributed to an imposed constraint. In contrast, the consistency achieved here emerges from independently retrieved components, indicating that the model has learned a physically coherent relationship between ε and T_e. This provides additional confidence in the reliability and interpretability of both retrieved variables.

Taken together, these results indicate that the $\varepsilon \cdot T_e$ errors are comparable to the AMSR2 channel noise levels (NEΔT; Table 1) and are within the range required for practical downstream applications. Moreover, across ε, T_e and $\varepsilon \cdot T_e$, the validation and test statistics are in excellent agreement (Table 3), indicating robust generalization with no evidence of overfitting. This assessment is further supported from the observation-space validation in Section 4.2.

4.2 Observation-space evaluation via radiative transfer closure

Because neither ε nor T_e has a direct observational reference, we validate the retrieval in observation space by propagating the retrieved sea-ice surface emission parameters through a radiative transfer model. Specifically, the ANN-retrieved ε and T_e are used as lower boundary conditions in RTTOV, together with collocated ERA5 atmospheric T/q profiles, to calculate TOA TBs. We then compare simulated TBs against AMSR2 observations. Agreement between simulated and observed TBs is not guaranteed a priori. The ANN is trained solely on a simulation-based dataset, and any radiative inconsistency in the retrieved surface parameters would directly manifest as discrepancies in the reconstructed TBs. This evaluation therefore provides an independent and physically grounded assessment of retrieval performance. An additional internal consistency check is provided by the 23H channel, which is excluded from the ANN input vector. Retrieval skill at 23H thus reflects the algorithm's ability to reconstruct this channel through cross-channel radiative relationships, rather than through direct channel-wise fitting.

Assessment is conducted over the Arctic Ocean north of 70°N with SIC ≥ 95% for all DJF seasons from 2012/2013 through 2024/2025. Figure 6 shows scatterplots of simulated versus observed TBs and deviation histograms (here ΔTB = simulated TB – observed TB), while Table 4 summarizes statistics (linear correlation coefficient r, mean deviation b, and standard deviation σ) for the full period and for individual winters. Over 13 winter seasons, simulated TBs cluster tightly around the 1:1 line for all channels (r ≈ 0.99) with near-Gaussian deviation distributions and spreads on the order of ~1 K. Importantly, this close agreement also extends to the 23H channel, which is not included in the ANN input vector, indicating that its reconstruction arises from cross-channel radiative consistency rather than direct fitting. Mean deviations are small for most channels (typically within ±0.2 K), while more systematic offsets appear in H polarization, most notably a negative bias at 23H (−0.81 K) and a positive bias at 36H (0.64 K).

https://doi.org/10.5194/essd-2026-471
Preprint. Discussion started: 24 August 2026

Open Access Earth System Science Data Discussions

Table 4. Retrieval validation statistics with AMSR2 TOA TB at six target channels (18V/H, 23V/H, 36V/H) for DJF 2012/2013–2024/2025 over the Arctic Ocean (north of 70°N; SIC ≥ 95%): linear correlation coefficient (r), mean deviation (b; simulation − observation), and standard deviation (σ) for the full record and for individual winters.

Year (DJF)	18V			23V			36V			18H			23H			36H		
	r	b	σ	r	b	σ	r	b	σ	r	b	σ	r	b	σ	r	b	σ
All	0.99	−0.06	1.06	0.99	−0.20	1.05	0.99	−0.02	1.12	0.99	0.07	0.91	0.99	−0.81	1.27	0.99	0.64	1.18
2012–2013		0.27	1.24		0.05	1.18		0.39	1.18		0.44	1.14		−0.46	1.3		1.12	1.29
2013–2014		0.06	1.14		0.06	1.20		0.18	1.25		0.27	1.00		−0.29	1.59		1.11	1.41
2014–2015		0.10	1.27		−0.04	1.34		0.17	1.25		0.19	1.11		−0.66	1.51		0.86	1.36
2015–2016		−0.00	1.08		−0.20	1.12		−0.14	1.28		0.03	1.02		−0.75	1.51		0.86	1.33
2016–2017		−0.19	1.18		−0.45	1.14		−0.16	1.22		−0.05	0.94		−1.27	1.19		0.22	1.22
2017–2018		−0.11	0.99		−0.17	0.92		−0.09	1.13		0.09	0.76		−0.67	1.16		0.81	1.09
2018–2019		−0.02	1.09		−0.09	1.09		0.10	1.06		0.18	0.91		−0.75	1.26		0.64	1.19
2019–2020		−0.19	1.04		−0.39	0.98		−0.26	1.12		−0.10	0.91		−1.02	1.16		0.48	1.08
2020–2021		−0.17	1.15		−0.42	1.11		−0.10	1.10		−0.03	0.90		−1.11	1.18		0.36	1.10
2021–2022		−0.13	1.06		−0.19	0.98		−0.15	1.14		−0.01	0.87		−0.70	1.09		0.69	1.05
2022–2023		−0.12	1.01		−0.13	1.02		0.15	1.00		0.09	0.97		−0.79	1.28		0.65	1.12
2023–2024		−0.10	0.97		−0.25	0.97		−0.03	1.04		−0.07	0.83		−1.03	1.16		0.43	1.10
2024–2025		−0.15	1.03		−0.29	1.03		−0.23	1.14		−0.02	0.82		−0.93	1.35		0.25	1.18

https://doi.org/10.5194/essd-2026-471
Preprint. Discussion started: 24 August 2026

Open Access Earth System Science Data Discussions

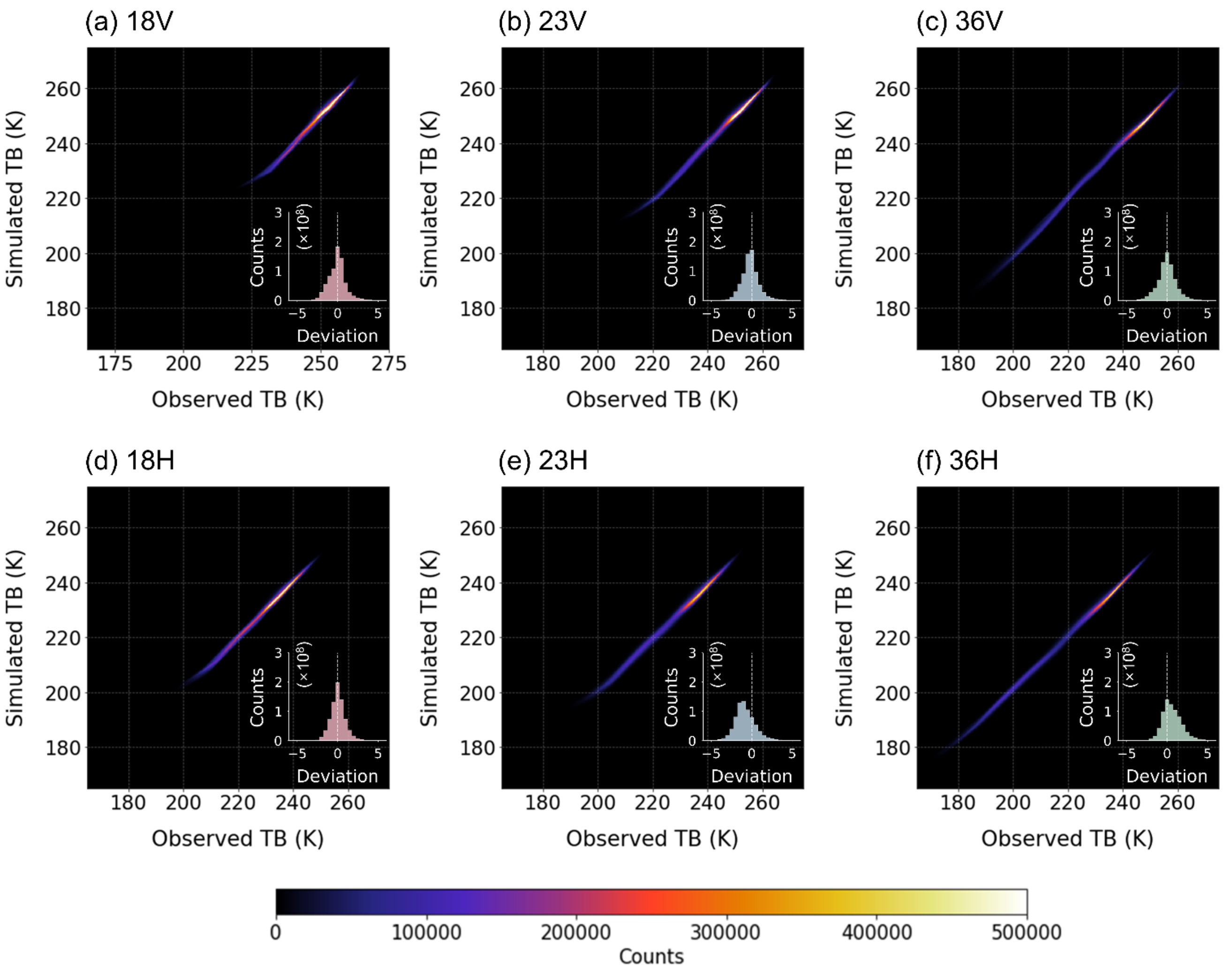

Figure 6. Scatterplots of simulated versus observed channel-wise TOA TBs across DJF 2012/2013–2024/2025 over the Arctic Ocean (north of 70°N; SIC ≥ 95%), with deviation histograms (simulation – observation).

Seasonal statistics are stable across the AMSR2 record (Fig. 7a and Table 4). Bias remains close to neutral for V polarization along with 18H (e.g., 18V: −0.19 to 0.27 K, 23V: −0.45 to 0.06 K, 36V: −0.26 to 0.39 K, 18H: −0.10 to 0.44 K), whereas persistent offsets are mainly confined to 23H (negative, −1.27 to −0.29 K) and 36H (positive, 0.22 to 1.12 K). For all channels, the spreads remain bounded and consistent from winter to winter (σ ≈ 1.0 to 1.6 K, with the largest values at 23H; see Table 4). Daily diagnostics (Fig. 7b) show no abrupt day-to-day discontinuities and no evidence of systematic drift in deviation characteristics over time, indicating that the retrieval is temporally robust and stable over the full AMSR2 record without the need for retraining or parameter adjustment.

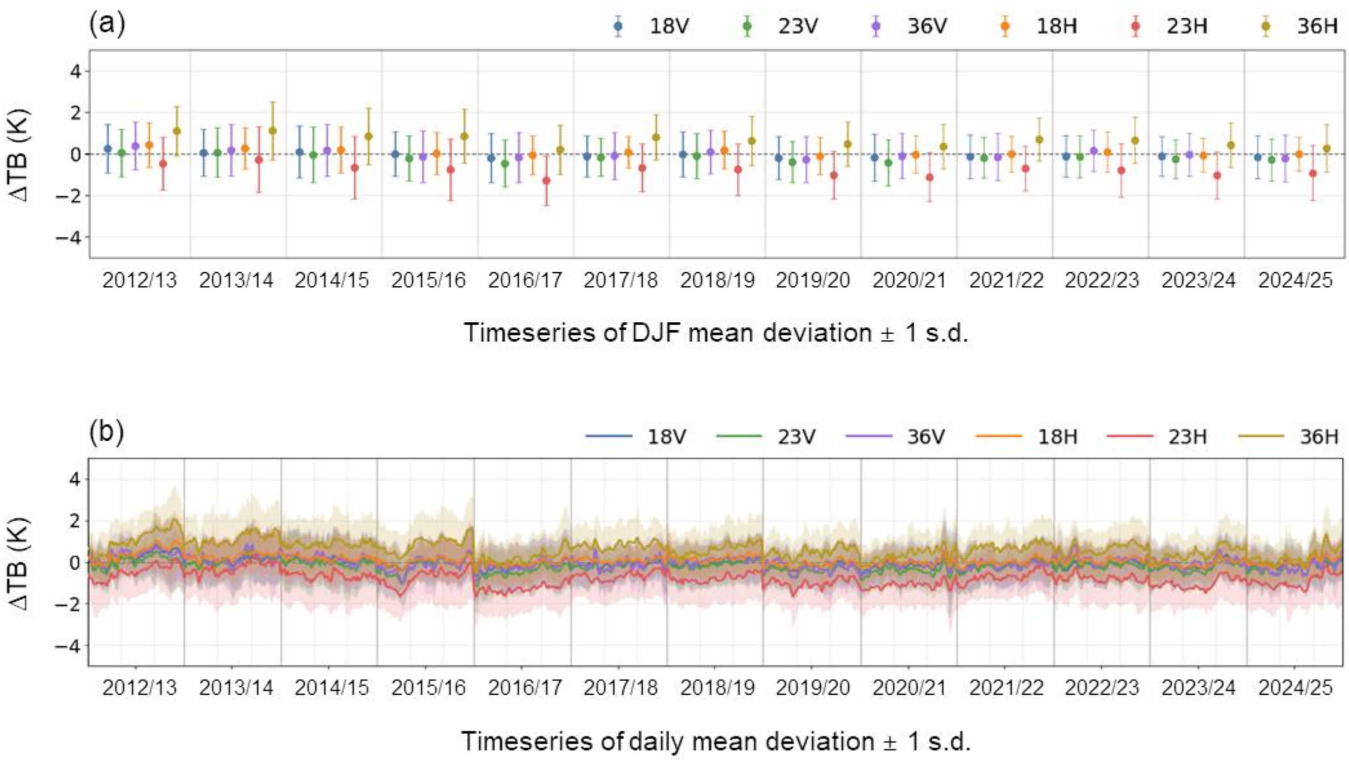

Figure 7. Temporal stability of observation-space deviations (simulation – observation) for DJF 2012/2013–2024/2025 over the Arctic Ocean (north of 70°N; SIC ≥ 95%): (a) winter-by-winter means ±1 s.d. and (b) day-to-day means ±1 s.d.

5 Comparison with existing emissivity products and sea-ice-type-dependent characteristics

To put the present retrieval in context, we compare it with commonly used emissivity products. This comparison is not intended as a validation, because the compared quantities are defined differently. Instead, it aims to clarify how differences in physical assumptions, particularly the treatment of emission depth, affect the resulting emissivity estimates. The comparison is conducted over the Arctic Ocean north of 70°N with SIC ≥ 95% for January 2023 across six AMSR2 window channels (18.7V/H, 23.8V/H, and 36.5V/H; Figs. 8–9). The products considered here are not directly interchangeable, as they represent distinct boundary definitions:

(i) Penetration-aware emissivity (ε; this study): Our retrieval estimates emissivity associated with subsurface emission, representing radiation emerging from within the sea-ice medium under microwave penetration effects. It is therefore interpreted as a penetration-aware emissivity. The corresponding temperature is the emission temperature T_e, reflecting a depth-weighted thermal state.

https://doi.org/10.5194/essd-2026-471
Preprint. Discussion started: 24 August 2026

(ii) Effective emissivity (ε_{eff}): A commonly used top-down inversion approach derives an "effective" emissivity by rearranging the radiative transfer equation to match observed TOA TB using ancillary atmospheric T/q profiles and skin temperature T_s information (e.g., reanalysis). This inversion yields an emissivity that closes the radiative budget at the surface boundary (based on skin-emission assumption), rather than isolating subsurface radiative processes. Using Eq. (1), rearranging for ε_{eff} yields

$$\varepsilon_{\mathrm{eff},i} = \frac{\left(\dfrac{TB_{\mathrm{i}} - TB_{\mathrm{i}}^{\uparrow}}{\Upsilon_{\mathrm{i}}}\right) - TB_{\mathrm{i}}^{\downarrow}}{T_s - TB_{\mathrm{i}}^{\downarrow}} \tag{13}$$

(iii) Climatological effective emissivity (ε^{TEL}; TELSEM2): This provides a monthly emissivity atlas built from historical observation-anchored inversions and temporal aggregation (Section 2.2.5). For a given month m and location x, it represents a climatological mean state of ε_{eff} as follows:

$$\varepsilon_{\mathrm{i}}^{\mathrm{TEL}}(x,m) = \frac{1}{N(x)} \sum \varepsilon_{\mathrm{eff,i}}(x,m) \tag{14}$$

where x denotes location and N is the number of multi-year samples. Thus it is a climatological prior rather than a scene-specific estimate.

The origin of systematic differences among these products lies in the treatment of microwave penetration. In winter Arctic conditions, emission in window channels is not purely skin-originated, and the relevant temperature is a subsurface-weighted bulk temperature T_e. Under this framework, the emitted signal can be expressed as

$$\varepsilon_{\mathrm{eff},i} T_s = \varepsilon_{\mathrm{i}} T_{e,\mathrm{i}} \tag{15}$$

or equivalently,

$$\varepsilon_{\mathrm{eff},i} = \varepsilon_{\mathrm{i}} \frac{T_{e,\mathrm{i}}}{T_s} \tag{16}$$

In the winter Arctic, strong surface cooling and snow insulation typically produce $\partial T/\partial z > 0$ (depth z positive downward), so deeper layers are warmer and $T_e > T_s$ is common. Consequently, ε_{eff} tends to exceed ε when penetration is deeper and vertical thermal gradient is higher.

The comparison of monthly mean emissivity for January 2023 (Figs. 8–9) shows that all three products capture the expected first-order behavior. V-pol emissivity is higher than H-pol at a given frequency and emissivity generally decreases from 18 to

https://doi.org/10.5194/essd-2026-471
Preprint. Discussion started: 24 August 2026

36 GHz. All products also share coherent regional structure consistent with known sea-ice regimes (e.g., MYI sectors near the Canadian Arctic Archipelago and Greenland versus broader FYI sectors), with contrasts sharpening toward 36 GHz. Differences follow product definitions. ε_{eff} often shows near-unity or higher (blackbody-like) values (e.g., Geer, 2024; Kilic et al., 2025), particularly at low frequencies, in V polarization, and over FYI sector, reflecting closure under the skin-emission assumption when $T_e > T_s$. TELSEM2 preserves broad spatial organization but appears smoother owing to the construction of the monthly climatology, which can suppress scene-specific features and year-to-year regime shifts.

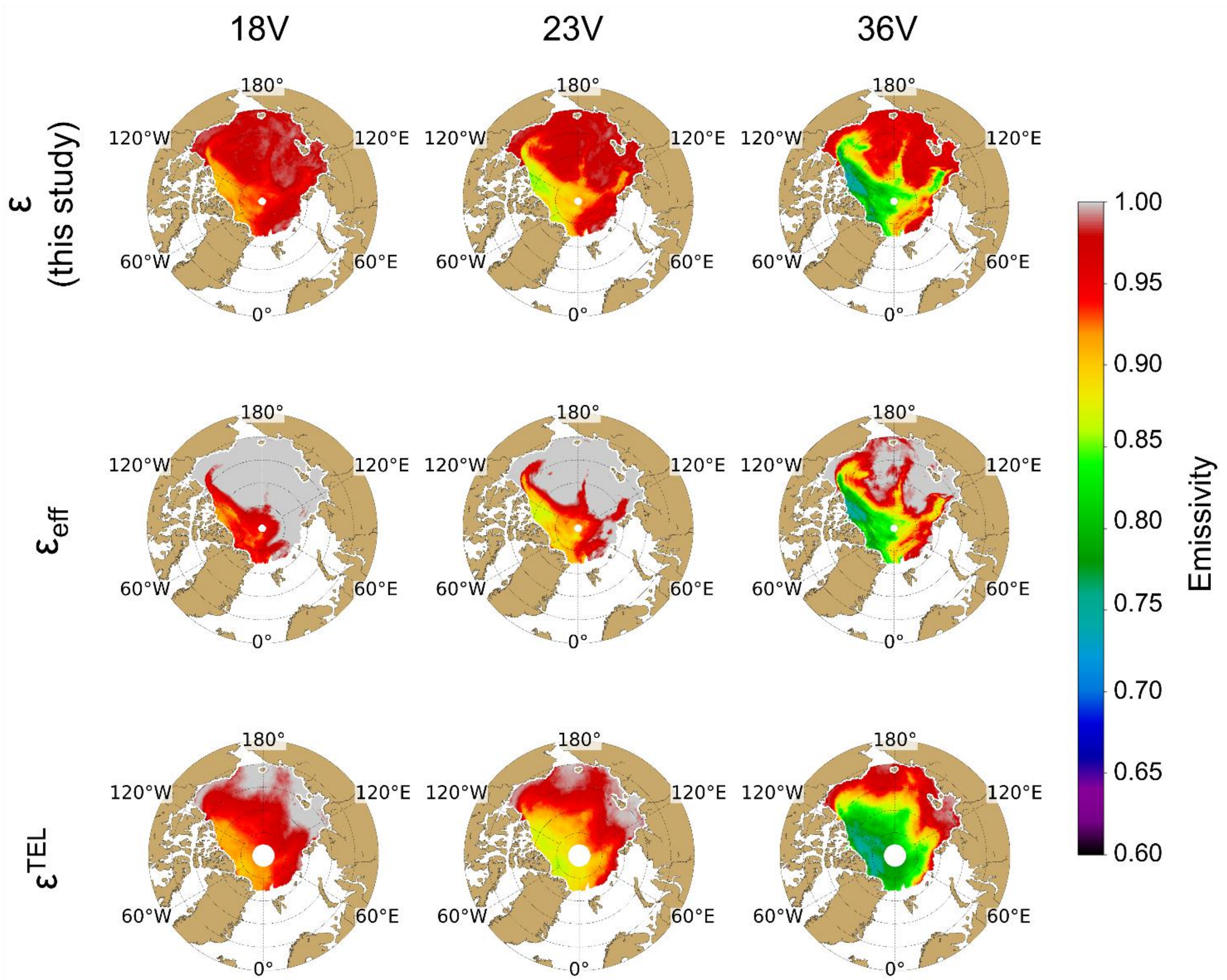

Figure 8. January 2023 monthly-mean emissivity maps over Arctic Ocean (north of 70°N; SIC ≥ 95%). Columns correspond, from left to right, to the six target channels: 18V, 23V, and 36V. Rows show the penetration-aware emissivity ε (this study), the effective emissivity ε_{eff}, and climatological effective emissivity ε^{TEL} (TELSEM2), respectively.

https://doi.org/10.5194/essd-2026-471
Preprint. Discussion started: 24 August 2026

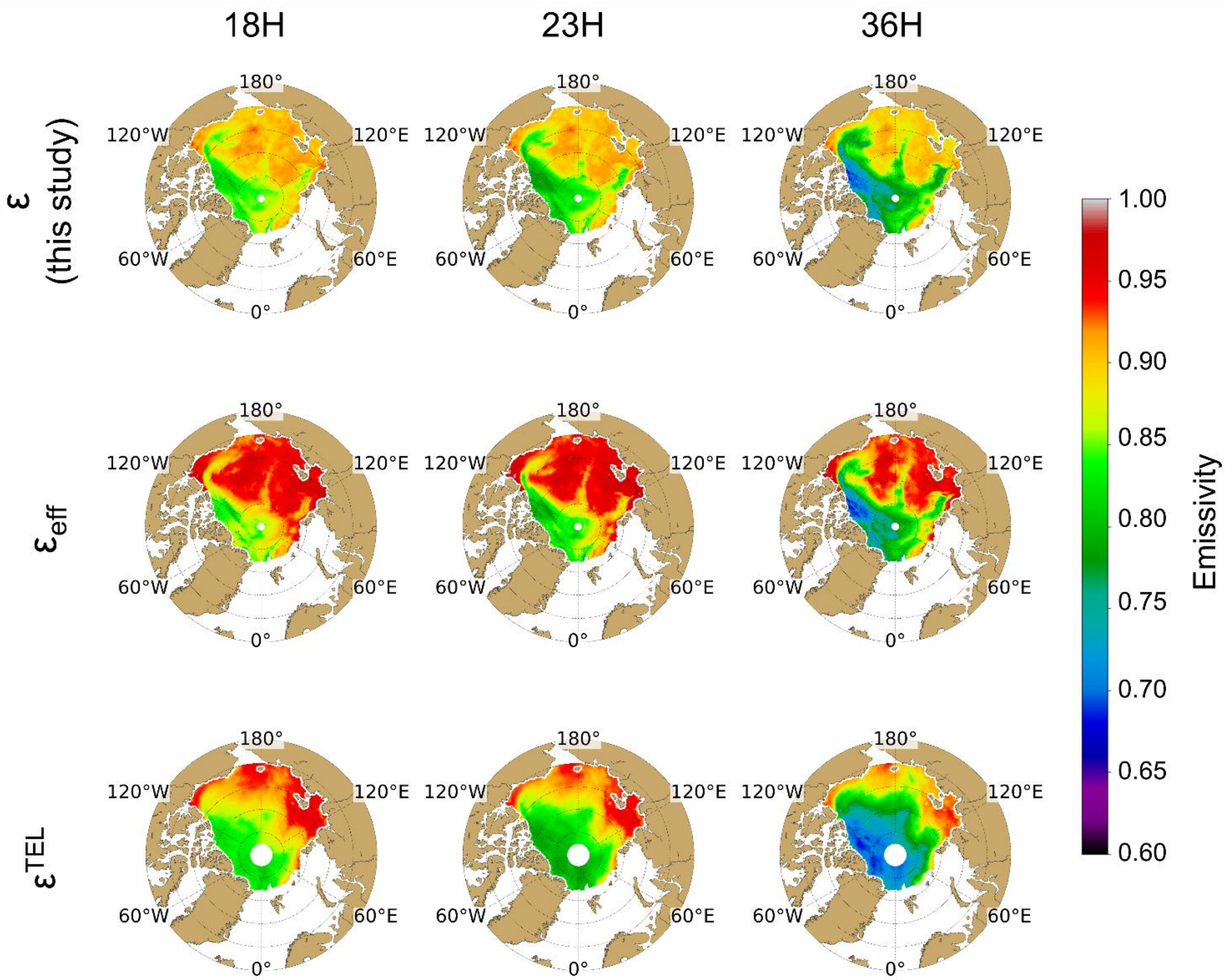

Figure 9. As Figure 8, but for 18H, 23H, and 36H.

545 Histogram comparisons (Fig. 10) reinforce these points. Across products, V-pol distributions are right-shifted and more skewed than H-pol, and increasing frequency broadens distributions and shifts them downward. Within this structure, ε_{eff} is generally right-shifted (higher), ε^{TEL} is left-shifted (lower) in several channels, and the retrieved ε often lies between them. A distinct low-emissivity accumulation in TELSEM2 is consistent with its historical sampling, which may retain signatures of a past Arctic with a broader MYI footprint than today's increasingly FYI-dominated Arctic under global warming.

https://doi.org/10.5194/essd-2026-471
Preprint. Discussion started: 24 August 2026

Open Access Earth System Science Data Discussions

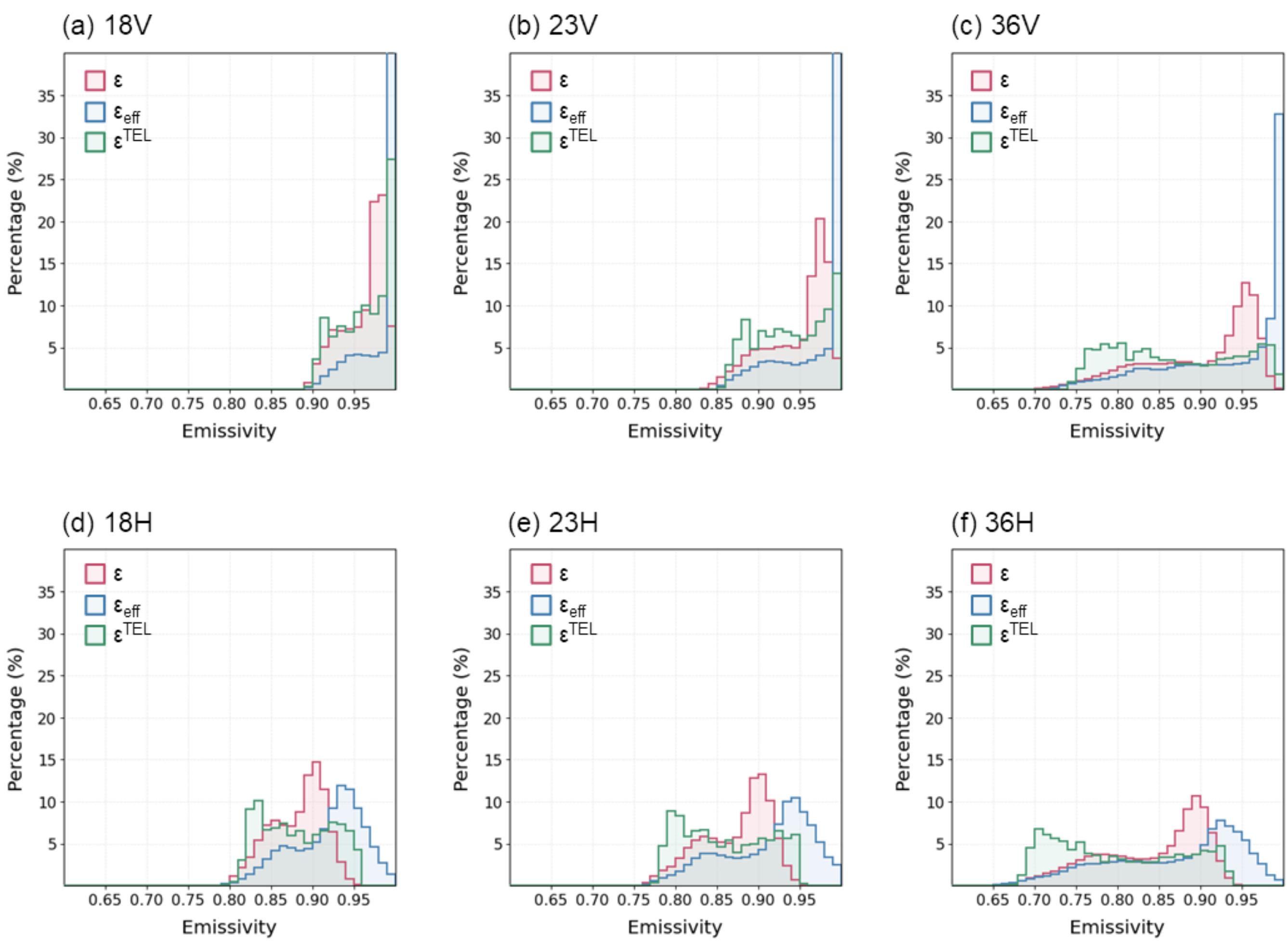

Figure 10. Histograms of Arctic emissivity in January 2023 (north of 70°N; SIC ≥ 95%) for six target channels, comparing penetration-aware emissivity ε (this study), effective emissivity ε_{eff}, and climatological effective emissivity ε^{TEL} (TELSEM2).

Overall, ε_{eff} is useful for observation-space closure with T_s but can fold penetration effects into an inflated emissivity and may inherit sensitivities to ancillary information. TELSEM2 provides a stable observation-anchored climatological prior but may under-represent present-day, scene-dependent variability. By design, the retrieved ε targets subsurface-influenced emission while preserving cross-channel consistency, which is advantageous for radiative-transfer calculations and downstream applications (e.g., data assimilation) that require internally consistent lower boundary conditions.

To further assess the physical consistency of the retrieval, we examined whether the retrieved ε preserves the expected radiative characteristics of FYI and MYI. Because FYI and MYI differ substantially in their internal structure and properties, they should exhibit distinguishable emissivity distributions. The retrieved ε fields for January 2023 were collocated with the daily OSI

https://doi.org/10.5194/essd-2026-471
Preprint. Discussion started: 24 August 2026

SAF sea-ice type product and classified into FYI and MYI over the Arctic Ocean. We then compared the normalized ε distributions for the two sea-ice types across the six target channels and quantified their separation using the overlap coefficient (OVL), defined as the shared fraction of the two PDFs (Fig. 11). The OVL ranges from 0 for completely separated distributions to 1 for identical distributions, with smaller values indicating a clearer separation between the two ice-type regimes.

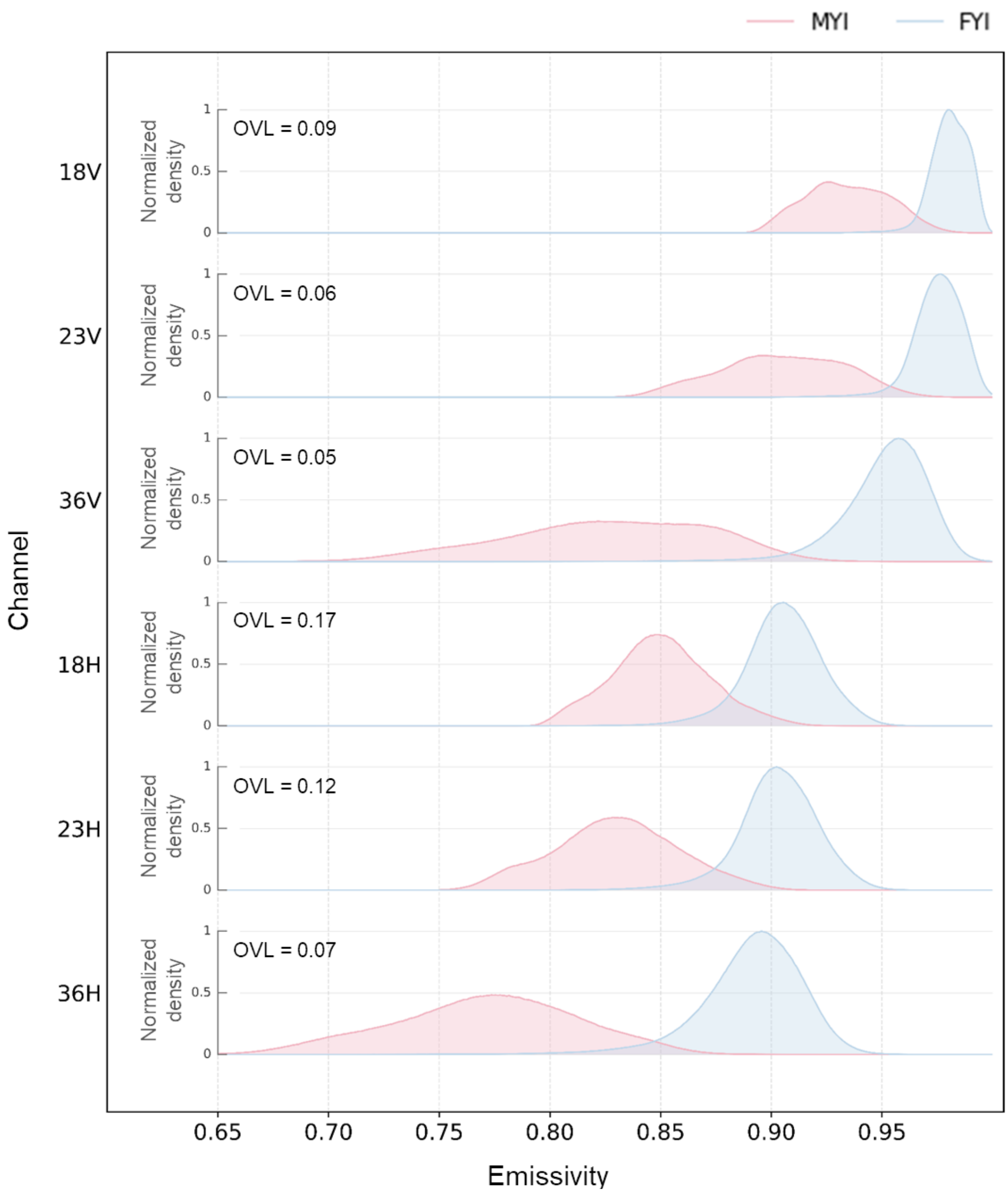

565 **Figure 11.** Normalized distributions of retrieved penetration-aware sea-ice emissivity (ε) over the Arctic Ocean (north of 70°N; SIC ≥ 95%) in January 2023 for first-year sea ice (FYI; blue) and multiyear sea ice (MYI; red) at the six target channels, with the overlap coefficient (OVL) shown in each panel.

The results show a robust FYI–MYI contrast across all target channels. FYI emissivities are concentrated at higher values, whereas MYI emissivities are shifted toward lower values and display relatively broader distributions, including pronounced low-emissivity tails at the higher frequencies. The separation is also quantitatively clear, with OVL values of only 0.05 to 0.17 across the channels. This result suggests that the retrieved ε can be used to distinguish between the two sea-ice types, particularly at the 23V and 36V channels, where the FYI and MYI distributions are most clearly separated. Together, these results demonstrate that the retrieved ε preserves the characteristic sea-ice-type-dependent microwave-emission signatures at the Arctic basin scale and retains information useful for distinguishing between FYI and MYI.

6 Observational assessment of retrieved sea-ice surface emission parameters

To evaluate the realism of the retrieved ε, we compare our estimates with published values (mean ± 1σ) reported separately for FYI and MYI at frequencies identical or close to the target channels of this study, including Comiso (1983), Winebrenner et al. (1992), Stroeve et al. (2006), Mathew et al. (2009), and Lee et al. (2017), together with ε_{eff} and ε^{TEL} (Fig. 12). For the present ε, ε_{eff} and ε^{TEL}, the comparison was conducted for January 2023, with FYI and MYI identified from the daily OSI SAF sea-ice type product and the corresponding monthly means and standard deviations calculated from the daily classified samples. Note that Winebrenner et al. (1992) and Stroeve et al. (2006) do not provide estimates around 23 GHz, and that Stroeve et al. (2006) and Lee et al. (2017) do not report emissivity variability (1σ).

This comparison should be interpreted with caution, because the available estimates are not fully consistent in frequency, period, or retrieval assumptions. Comiso (1983) and Mathew et al. (2009) both estimated T_e from empirical linear relationships of the form '$T_e = a \cdot T_s + b$' with bulk coefficients specified by season or month, but applied different emissivity formulations. Comiso (1983) derived emissivity from SMMR observations during 1978–1979 using the simplified radiative transfer relation '$\varepsilon = TB / T_e$', whereas Mathew et al. (2009) used AMSR-E observations for January 2005 within a framework analogous to Eq. (13). Lee et al. (2017) also used AMSR-E observations for January conditions during 2003–2011, but defined T_e as the snow/sea-ice interface temperature inferred from TBs at 6.9V/H using a combined Fresnel equation. Meanwhile, Winebrenner et al. (1992) and Stroeve et al. (2006) derived theoretical emissivities from field measurements collected during 1988–1990 and 2003 using the Fresnel half-space model and the Microwave model (MWMOD), respectively. Given these differences, the comparison is not intended to seek agreement in absolute magnitude, but to assess whether the present retrieval falls within the range reported in the literature and reproduces the common spectral, polarization, and ice-type dependences found in earlier studies.

That common structure appears clearly in the present retrieval. The emissivity is systematically higher for FYI than for MYI, higher in V-pol than in H-pol, only weakly frequency-dependent for FYI, and more strongly decreasing toward 36 GHz for MYI. For FYI, the retrieved ε are high and nearly spectrally flat, with V-pol values of 0.980±0.009, 0.975±0.011, and 0.952±0.020, and H-pol values of 0.905±0.017, 0.903±0.018, and 0.891±0.023 at 18.7, 23.8, and 36.5 GHz, respectively. For

600 MYI, the spectral dependence strengthens markedly, with V-pol values decreasing from 0.934±0.019 to 0.905±0.028 and 0.826±0.046, and H-pol values from 0.850±0.022 to 0.830±0.028 and 0.771±0.042. These estimates remain within the spread of other studies while preserving the characteristic FYI–MYI contrasts, V–H polarization differences, and spectral behavior of Arctic sea-ice microwave emission.

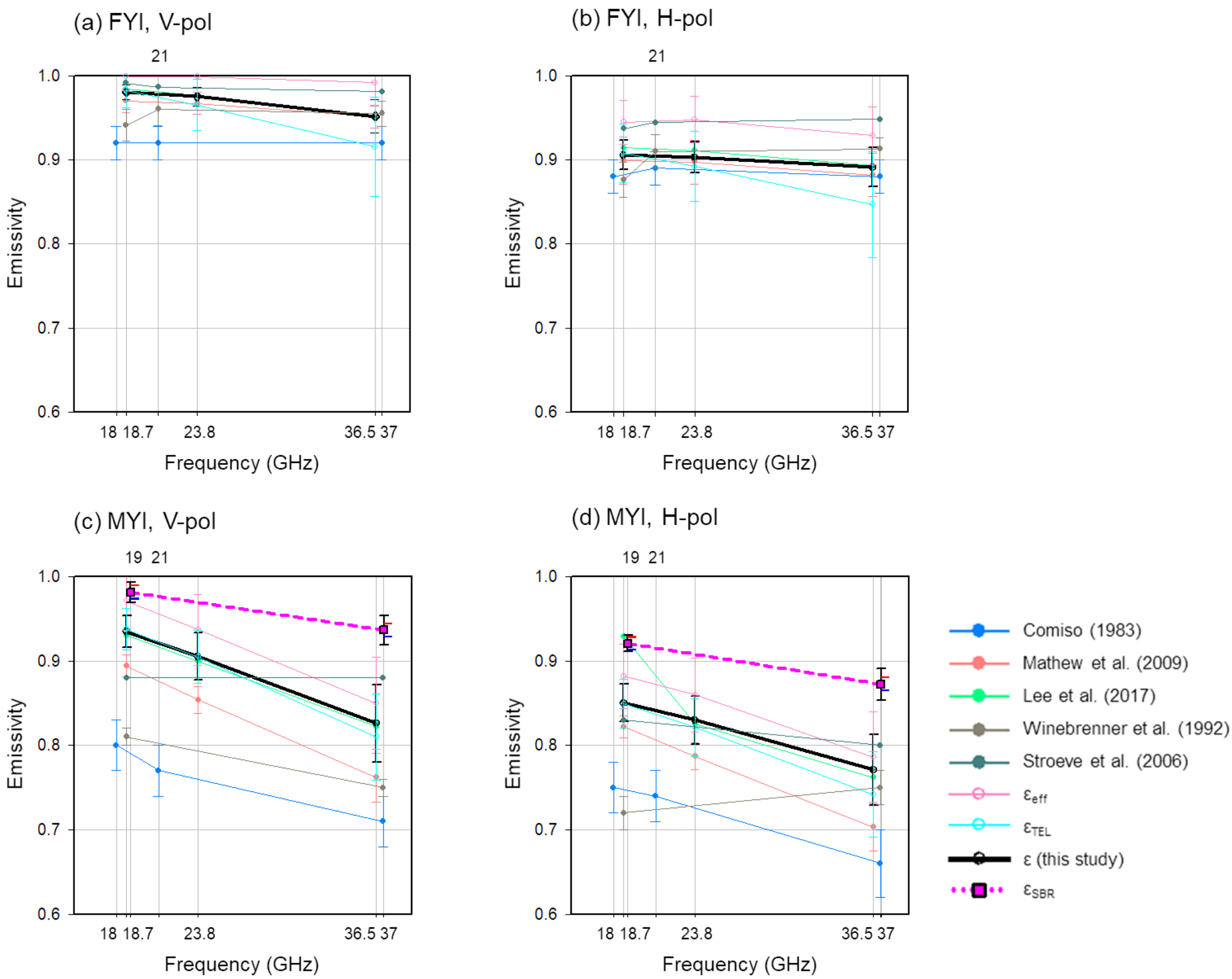

605 **Figure 12.** Comparison of emissivity estimates from this study with literature-based estimates for first-year sea ice (FYI) and multiyear sea ice (MYI) in vertical (V) and horizontal (H) polarizations. Mean ± 1 s.d. of (a) FYI, V-pol; (b) FYI, H-pol; (c) MYI, V-pol; and (d) MYI, H-pol. For UoM SRB-based emissivity (ε_{SBR}), the blue and red horizontal marks are sensitivity ranges of T_e ± 2 K, where T_e is the emission temperature obtained in this study.

https://doi.org/10.5194/essd-2026-471
Preprint. Discussion started: 24 August 2026

To provide a complementary field-based assessment, we analyzed quality-controlled TB measurements from UoM SBR collected during the MOSAiC expedition. Because the UoM SBR measures surface-leaving TBs (TB_{SBR}), the corresponding emissivity (ε_{SBR}) was estimated by inverting the surface-boundary radiative-transfer equation:

$$\varepsilon_{SBR} = \frac{TB_{SBR} - TB^{\downarrow}}{T_e - TB^{\downarrow}} \tag{17}$$

where $TB^{\downarrow}$ is the atmospheric down-welling emission TB and was calculated using RTTOV with ERA5 atmospheric T/q profiles. Because the emission signal of UoM SBR (TB_{SBR}) originates in the emission layer below the surface and there is no measurement of T_e, we used retrieved T_e from this study and additionally perturbed T_e by ± 2 K to quantify the sensitivity of the UoM SBR-derived emissivities. The resulting statistics and sensitivity ranges were overlaid on the MYI panels of Fig. 12(c)–(d) for comparison with the retrieved emissivities from this study and literature-based estimates. Because the MOSAiC site was dominated by second-year sea ice, we considered the sea-ice type to be MYI.

The UoM SBR-derived emissivity ranges are systematically higher than all other values, thereby appearing as outliers. Because the derived emissivities are directly sensitive to the radiometric accuracy of the measured TBs, this result motivated a further assessment of the radiometric performance of the UoM SBR measurements using AMSR2 observations as a reference. AMSR2 provides a well-calibrated and extensively validated microwave radiometric record and therefore is suitable for examining the radiometric consistency of the UoM SBR measurements.

To facilitate the radiometric consistency assessment, the UoM SBR surface-leaving TBs were converted to TOA-equivalent TBs (TB_{SBR}^{TOA}) using the following equation:

$$TB_{SBR}^{TOA} = \Upsilon \cdot TB_{SBR} + TB^{\uparrow} \tag{18}$$

where Υ is the total atmospheric transmittance and $TB^{\uparrow}$ is the upwelling atmospheric emission TB. Both quantities were calculated using RTTOV with ERA5 atmospheric T/q profiles. The resulting UoM SBR TOA TBs were then compared with collocated AMSR2 TBs (Fig. 13).

https://doi.org/10.5194/essd-2026-471
Preprint. Discussion started: 24 August 2026

Open Access Earth System Science Data Discussions

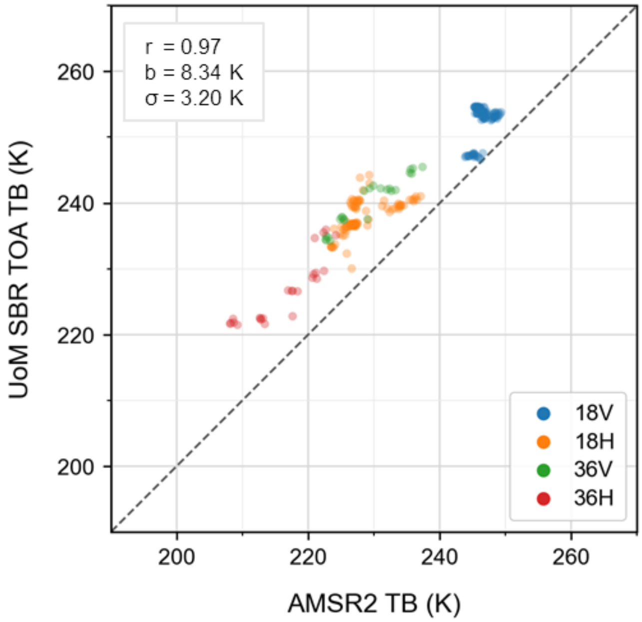

Figure 13. Scatterplot of AMSR2 brightness temperatures (TBs) and top-of-atmospheric (TOA)-equivalent UoM SBR TBs.

The TOA-space comparison shows a high correlation ($r = 0.97$) and a residual spread of about 3 K across the target channels, indicating that the two datasets capture similar radiometric variability. However, the comparison also reveals a systematic TB deviation of approximately 6.17–11.97 K, although the 18 GHz V-pol channel exhibits a smaller bias than the other channels. Several factors may contribute to this discrepancy, including differences in instrument characteristics, channel center frequencies, spatial representativeness, and data-processing procedures.

Nevertheless, the largely uniform nature of the bias for each channel suggests that the discrepancy is broadly consistent with an offset-type calibration difference. In microwave radiometry, TB calibration is commonly expressed as a linear function of the measured digital counts (C), i.e., $TB = C_0 + \alpha\, C$ where C_0 is an offset count and α is a calibration coefficient. Motivated by this interpretation, we applied channel-dependent mean-offset adjustments based on the comparison with collocated AMSR2 observations before comparing our products with UoM SBR measurements. After accounting for atmospheric contributions, the corresponding surface-level adjustments were 6.17 and 9.87 K for the 18 GHz V/H-pols, respectively, and 11.97 and 11.18 K for the 36 GHz V/H-pols, respectively. The mean-offset-adjusted UoM SBR TBs were subsequently used to assess the retrieved sea-ice surface emission parameters.

Because the UoM SBR provides surface-leaving TBs rather than independent estimates of $\{\varepsilon, T_e\}$, we perform the comparison in surface-emission space. This avoids introducing an additional assumption regarding the unobserved T_e, required to derive UoM SBR-based emissivity. Specifically, we reconstructed the equivalent surface-leaving TBs ($TB^{sfc\text{-}leaving}$) with retrieved $\{\varepsilon, T_e\}$ pairs as follows:

https://doi.org/10.5194/essd-2026-471
Preprint. Discussion started: 24 August 2026

$$TB^{sfc-leaving} = TB^{\downarrow}\left(1-\varepsilon\right)+\varepsilon T_e \tag{19}$$

650 where $TB^{\downarrow}$ was calculated using RTTOV with ERA5 atmospheric T/q profiles.

As shown in Fig. 14, the surface-leaving TBs from this study agree closely with the mean-offset-adjusted UoM SBR TBs, yielding $r = 0.96$, $b \approx -0.5$ K, and $\sigma \approx 3$ K. Given that the UoM SBR measurements provide an independent estimate of surface-leaving microwave emission, this agreement indicates that the retrieved $\{\varepsilon, T_e\}$ pair reproduces realistic surface radiative boundary conditions over Arctic sea ice. The field-based results therefore provide additional observational support for the
655 physical consistency and realism of the retrieved dataset.

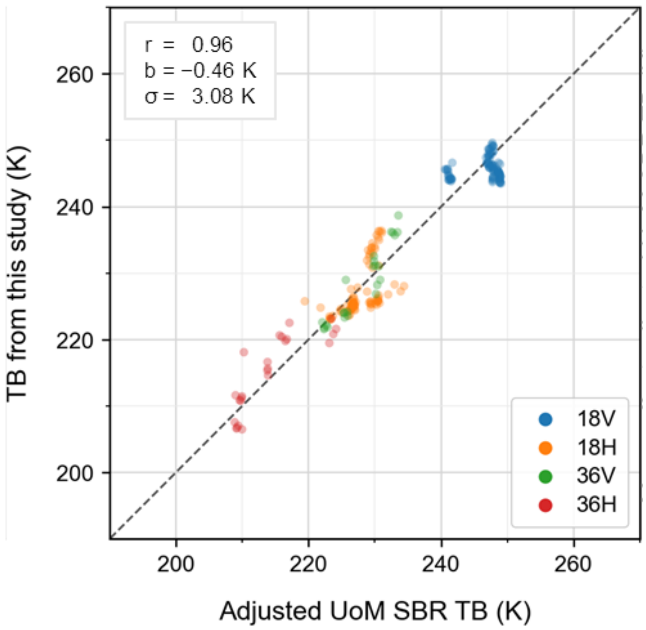

Figure 14. Scatterplot of surface-leaving brightness temperatures (TBs) from this study and mean-offset-adjusted UoM SBR TBs.

7 Data availability

660 The data described in this manuscript will be publicly available in NetCDF format from an open-access repository upon publication. During peer review, anonymous repository-hosted access is provided through a temporary data-in-review link via Zenodo repository (Kang, 2026; https://tinyurl.com/5n6843r8). The final dataset is derived from AMSR2 Level-1 swath observations and distributed as daily-mean fields on a 25 km polar stereographic grid (304 × 448). The archive covers the boreal winter months (DJF) from December 2012 to February 2025 over the Arctic Ocean north of 70°N under compact sea-

https://doi.org/10.5194/essd-2026-471
Preprint. Discussion started: 24 August 2026

ice conditions (SIC ≥ 95%). Each file contains six sea-ice emissivity (ε) fields at 18, 23, and 36 GHz in V/H polarizations, three corresponding emission temperature (T_e) fields at 18, 23, and 36 GHz, and the associated time, longitude, latitude, and SIC fields. Emissivity is bounded between 0 and 1, emission temperature remains below the freezing point of seawater, and missing values are assigned as −9999.

The simulation-based training dataset is also available through the same repository (Kang, 2026; https://tinyurl.com/5n6843r8). It is distributed as a single file organized along a single point dimension of length N = 1,028,610. The file contains fourteen variables: five simulated TOA TBs used as predictors (18 GHz V/H, 23 GHz V, 36 GHz V/H; K), and six ε (18, 23, and 36 GHz in V and H polarization; dimensionless) and three T_e (18, 23, and 36 GHz; K) used as targets. Because every sample is generated from a complete set of surface and atmospheric inputs, the file contains no missing value.

The other datasets used in this study are publicly available from their respective sources: AMSR2 TBs from the JAXA G-Portal (JAXA, n.d.; https://gportal.jaxa.jp/gpr); ERA5 atmospheric T/q profiles along with SIC from the Copernicus Climate Data Store (Hersbach et al., 2023a, b; https://doi.org/10.24381/cds.bd0915c6; https://doi.org/10.24381/cds.adbb2d47); OSI SAF sea-ice type from OSI SAF repository (OSI SAF, 2017; https://doi.org/10.15770/EUM_SAF_OSI_NRT_2006); UoM SBR TBs from PANGAEA (Rostosky et al., 2023; https://doi.org/10.1594/PANGAEA.956108); TELSEM2 as part of the RTTOV framework (NWP SAF, n.d.; https://nwp-saf.eumetsat.int/site/software/rttov/download/).

8 Conclusions

This study presents an Arctic winter data record of sea-ice surface emission parameters derived from AMSR2 observations, spanning 13 winter seasons from DJF 2012/2013 to DJF 2024/2025. Constructed using an ANN retrieval algorithm trained on model-based simulation pairs of (TOA TBs vs. {ε, T_e}), the dataset provides channel-dependent emissivity and corresponding emission temperature for the low-frequency microwave window channels at 18, 23, and 36 GHz in both V/H polarizations, thereby establishing a spatiotemporally consistent record of surface parameters over the Arctic. In particular, the retrieval reflects the effects of the vertically heterogeneous, non-isothermal snow/sea-ice medium on microwave penetration, absorption, and emission, making the dataset more directly linked to the thermodynamic and radiative structure of the snow/sea-ice system than existing products. The record is also constructed to preserve consistency across frequencies and polarizations, providing an internally coherent description of sea-ice emission.

Across the full record period, the retrieved variables reproduce observed AMSR2 TBs with near 1:1 agreement, approximately 1 K-level spreads, and stable season-to-season statistics. The retrieval also preserves inter-channel relationships across frequencies and polarizations, as demonstrated by the successful reconstruction of the 23H channel, although 23H was not directly constrained by the input vector. These results indicate that the algorithm captures physically meaningful radiative relationships among channels rather than relying on channel-specific fitting, and further support the robustness of the dataset for multi-winter application. A key feature of the present framework is that emissivity and emission temperature are retrieved

https://doi.org/10.5194/essd-2026-471
Preprint. Discussion started: 24 August 2026

independently, without imposing an explicit constraint on their coupled product. Despite this, their product $\varepsilon \cdot T_e$, which represents the surface emission term in the radiative transfer equation, shows excellent agreement with references. This consistency provides additional evidence that the retrieval preserves physically coherent relationships between radiative and thermodynamic properties, enhancing confidence in both variables.

Comparison with commonly used emissivity products further highlights that the present dataset represents a fundamentally different physical quantity. Unlike effective emissivity ε_{eff}, derived from radiative closure using prescribed skin temperature T_s, the retrieved emissivity ε here is penetration-aware and linked to subsurface emission processes. As a result, systematic differences between products can be interpreted in terms of vertical temperature gradients and microwave penetration depth within sea ice, rather than retrieval error alone. Independent comparison against ground-based radiometer measurements showed high correlations and relatively limited residual spreads across all target channels, indicating a reasonable level of agreement. Although this comparison does not constitute a strict footprint-scale validation, it provides observational support that the retrieval framework captures the observed variability in microwave emission over sea ice.

Overall, this dataset provides an interpretable, penetration-aware, and cross-channel-consistent characterization of the Arctic winter sea-ice radiative state through the paired $\{\varepsilon, T_e\}$ fields. Unlike conventional diagnostics based on TB contrasts or backscattering, it directly describes the penetration-weighted surface emission of the snow/sea-ice system and therefore contains information on both its radiative and thermodynamic state. Because emissivity and emission temperature are provided as a physically linked parameter pair, the dataset can serve as a reusable geophysical description of Arctic sea ice rather than merely an intermediate retrieval product. Potential applications include microwave radiative-transfer modeling, satellite retrieval development, inter-sensor consistency studies, data assimilation, and the interpretation of long-term satellite records of Arctic sea-ice variability and climate change. The framework is not specific to AMSR2 and can be retrained for other conical-scanning radiometer configurations, as well as for integrating physically consistent machine-learning retrievals into Earth-system observation and modeling.

Author contributions

EJK conceptualized the study, designed the methodology, developed the software, carried out the analysis and visualization, and wrote the original draft of the manuscript. **BJS** supervised the research, provided resources, and contributed to the review and editing of the manuscript. **HJS** and **CL** contributed to the review and editing of the manuscript. **WK** curated the data and contributed to the review and editing of the manuscript. **EJK** and **HJS** acquired funding. All authors contributed to the final version of the manuscript.

Competing interests

The authors declare that they have no conflict of interest.

Acknowledgements

The authors sincerely acknowledge the Numerical Modeling Center of the Korea Meteorological Administration (KMA) for its support of the research environment that made this study possible.

Financial support

This research was supported by the Basic Science Research Program through National Research Foundation of Korea (NRF) funded by the Ministry of Education (RS-2025-02633368), and the Global - Learning & Academic research institution for Master's·PhD students, and Postdocs (LAMP) Program through NRF funded by the Ministry of Education (RS-2023-00301914)

References

Aaboe, S., Down, E. J., and Eastwood, S.: Algorithm theoretical basis document for the global sea-ice edge and type product: GBL SIE OSI-402-d and GBL SIT OSI-403-d, Version 3.4, Ocean and Sea Ice Satellite Application Facility, https://osisaf-hl.met.no/sites/osisaf-hl/files/baseline_document/osisaf_cdop3_ss2_atbd_sea-ice-edge-type_v3p4.pdf (last access: 4 June 2026), 2021.

Al Jassar, H. K., Harris, A., and Ridley, J.: Retrieval of microwave surface emissivities using multi-sensor satellite remote sensing, in: IGARSS '95 – 1995 International Geoscience and Remote Sensing Symposium, Quantitative Remote Sensing for Science and Applications, Vol. 2, 1189–1191, https://doi.org/10.1109/IGARSS.1995.521180, 1995.

Aires, F., Prigent, C., Bernardo, F., Jiménez, C., Saunders, R., and Brunel, P.: A tool to estimate land-surface emissivities at microwave frequencies (TELSEM) for use in numerical weather prediction, Q. J. Roy. Meteor. Soc., 137, 690–699, https://doi.org/10.1002/qj.803, 2011.

Anderson, E. A.: A point energy and mass balance model of a snow cover, NOAA Technical Report NWS 19, National Oceanic and Atmospheric Administration, National Weather Service, 150 pp., https://repository.library.noaa.gov/view/noaa/6392 (last access: 4 June 2026), 1976.

Baek, S. H., Kang, E.-J., Sohn, B.-J., Kim, S.-W., and Shi, H.: Development of ANN-based algorithm to estimate wintertime sea ice temperature profile over the Arctic Ocean, IEEE T. Geosci. Remote, 61, 4302117, https://doi.org/10.1109/TGRS.2023.3293137, 2023.

Bauer, P., Moreau, E., Chevallier, F., and O'Keeffe, U.: Multiple-scattering microwave radiative transfer for data assimilation applications, Q. J. Roy. Meteor. Soc., 132, 1259–1281, https://doi.org/10.1256/qj.05.153, 2006.

Bell, B., Hersbach, H., Simmons, A., Berrisford, P., Dahlgren, P., Horányi, A., Muñoz-Sabater, J., Nicolas, J., Radu, R., Schepers, D., Soci, C., Villaume, S., Bidlot, J.-R., Haimberger, L., Woollen, J., Buontempo, C., and Thépaut, J.-N.: The ERA5 global reanalysis: Preliminary extension to 1950, Q. J. Roy. Meteor. Soc., 147, 4186–4227, https://doi.org/10.1002/qj.4174, 2021.

Belchansky, G. I., Douglas, D. C., Alpatsky, I. V., and Platonov, N. G.: Spatial and temporal multiyear sea ice distributions in the Arctic: A neural network analysis of SSM/I data, 1988–2001, J. Geophys. Res.-Oceans, 109, C10017, https://doi.org/10.1029/2004JC002388, 2004.

Bormann, N., Lupu, C., Geer, A., Lawrence, H., Weston, P., and English, S.: Assessment of the forecast impact of surface-sensitive microwave radiances over land and sea-ice, ECMWF Technical Memorandum No. 804, European Centre for Medium-Range Weather Forecasts, https://doi.org/10.21957/qyh34roht, 2017.

Bormann, N.: Accounting for Lambertian reflection in the assimilation of microwave sounding radiances over snow and sea-ice, Q. J. Roy. Meteor. Soc., 148, 2796–2813, https://doi.org/10.1002/qj.4337, 2022.

Cavalieri, D. J., Gloersen, P., and Campbell, W. J.: Determination of sea ice parameters with the Nimbus 7 SMMR, J. Geophys. Res.-Atmos., 89, 5355–5369, https://doi.org/10.1029/JD089iD04p05355, 1984.

Comiso, J. C.: Sea ice effective microwave emissivities from satellite passive microwave and infrared observations, J. Geophys. Res.-Oceans, 88, 7686–7704, https://doi.org/10.1029/JC088IC12P07686, 1983.

Comiso, J. C.: Characteristics of Arctic winter sea ice from satellite multispectral microwave observations, J. Geophys. Res., 91, 975–994, https://doi.org/10.1029/JC091iC01p00975, 1986.

Donlon, C. J., Martin, M., Stark, J., Roberts-Jones, J., Fiedler, E., and Wimmer, W.: The operational sea surface temperature and sea ice analysis (OSTIA) system, Remote Sens. Environ., 116, 140–158, https://doi.org/10.1016/j.rse.2010.10.017, 2012.

https://doi.org/10.5194/essd-2026-471
Preprint. Discussion started: 24 August 2026

Open Access Earth System Science Data Discussions

Fennig, K., Schröder, M., Andersson, A., and Hollmann, R.: A fundamental climate data record of SMMR, SSM/I, and SSMIS brightness temperatures, Earth Syst. Sci. Data, 12, 647–681, https://doi.org/10.5194/essd-12-647-2020, 2020.

Ferraro, R. R., Peters-Lidard, C. D., Hernandez, C., Turk, F. J., Aires, F., Prigent, C., Lin, X., Boukabara, S. A., Furuzawa, F. A., Gopalan, K., Harrison, K. W., Karbou, F., Li, L., Liu, C. T., Masunaga, H., Moy, L., Ringerud, S., Skofronick-Jackson, G. M., Tian, Y. D., and Wang, N. Y.: An evaluation of microwave land surface emissivities over the continental United States to benefit GPM-era precipitation algorithms, IEEE T. Geosci. Remote, 51, 378–398, https://doi.org/10.1109/TGRS.2012.2199121, 2013.

Fichefet, T. and Morales Maqueda, M. A.: Modelling the influence of snow accumulation and snow-ice formation on the seasonal cycle of the Antarctic sea-ice cover, Clim. Dynam., 15, 251–268, https://doi.org/10.1007/s003820050280, 1999.

Geer, A. J.: Simultaneous inference of sea ice state and surface emissivity model using machine learning and data assimilation, J. Adv. Model. Earth Sy., 16, e2023MS004080, https://doi.org/10.1029/2023MS004080, 2024.

Gloersen, P. and Barath, F.: A scanning multichannel microwave radiometer for Nimbus-G and SeaSat-A, IEEE J. Oceanic Eng., 2, 172–178, https://doi.org/10.1109/JOE.1977.1145331, 1977.

Gloersen, P. and Cavalieri, D. J.: Reduction of weather effects in the calculation of sea ice concentration from microwave radiances, J. Geophys. Res., 91, 3913–3919, https://doi.org/10.1029/JC091iC03p03913, 1986.

Grody, N. C.: Surface identification using satellite microwave radiometers, IEEE T. Geosci. Remote, 26, 850–859, https://doi.org/10.1109/36.7716, 1988.

Hersbach, H., Bell, B., Berrisford, P., Hirahara, S., Horányi, A., Muñoz-Sabater, J., Nicolas, J., Peubey, C., Radu, R., Schepers, D., Simmons, A., Soci, C., Abdalla, S., Abellan, X., Balsamo, G., Bechtold, P., Biavati, G., Bidlot, J., Bonavita, M., De Chiara, G., Dahlgren, P., Dee, D., Diamantakis, M., Dragani, R., Flemming, J., Forbes, R., Fuentes, M., Geer, A., Haimberger, L., Healy, S., Hogan, R. J., Hólm, E., Janisková, M., Keeley, S., Laloyaux, P., Lopez, P., Lupu, C., Radnoti, G., de Rosnay, P., Rozum, I., Vamborg, F., Villaume, S., and Thépaut, J.-N.: The ERA5 global reanalysis, Q. J. Roy. Meteor. Soc., 146, 1999–2049, https://doi.org/10.1002/qj.3803, 2020.

Hersbach, H., Bell, B., Berrisford, P., Biavati, G., Horányi, A., Muñoz Sabater, J., Nicolas, J., Peubey, C., Radu, R., Rozum, I., Schepers, D., Simmons, A., Soci, C., Dee, D., and Thépaut, J.-N.: ERA5 hourly data on pressure levels from 1940 to present, Copernicus Climate Change Service (C3S) Climate Data Store (CDS) [data set], https://doi.org/10.24381/cds.bd0915c6, 2023a.

https://doi.org/10.5194/essd-2026-471
Preprint. Discussion started: 24 August 2026

Earth System Science Data
Open Access Discussions

Hersbach, H., Bell, B., Berrisford, P., Biavati, G., Horányi, A., Muñoz Sabater, J., Nicolas, J., Peubey, C., Radu, R., Rozum, I., Schepers, D., Simmons, A., Soci, C., Dee, D., and Thépaut, J.-N.: ERA5 hourly data on single levels from 1940 to present, Copernicus Climate Change Service (C3S) Climate Data Store (CDS) [data set], https://doi.org/10.24381/cds.adbb2d47, 2023b.

Ivanova, N., Pedersen, L. T., Tonboe, R. T., Kern, S., Heygster, G., Lavergne, T., Sørensen, A., Saldo, R., Dybkjær, G., Brucker, L., and Shokr, M.: Inter-comparison and evaluation of sea ice algorithms: towards further identification of challenges and optimal approach using passive microwave observations, The Cryosphere, 9, 1797–1817, https://doi.org/10.5194/tc-9-1797-2015, 2015

Japan Aerospace Exploration Agency (JAXA): GCOM-W: AMSR2 standard products repository, G-Portal [data set], https://gportal.jaxa.jp/gpr (last access: 8 April 2026).

Jin, H., Chollet, F., Song, Q., and Hu, X.: AutoKeras: An AutoML library for deep learning, J. Mach. Learn. Res., 24, 1–6, https://www.jmlr.org/papers/v24/20-1355.html, 2023.

Jordan, R. E.: A one-dimensional temperature model for a snow cover: Technical documentation for SNTHERM.89, Special Report 91-16, U.S. Army Cold Regions Research and Engineering Laboratory, 49 pp., https://hdl.handle.net/11681/11677 (last access: 4 June 2026), 1991.

Jordan, R. E., Andreas, E. L., and Makshtas, A. P.: Heat budget of snow-covered sea ice at North Pole 4, J. Geophys. Res.-Oceans, 104, 7785–7806, https://doi.org/10.1029/1999JC900011, 1999.

Kang, E.-J., Sohn, B.-J., Tonboe, R. T., Dybkjær, G., Holmlund, K., Kim, J. M., and Liu, C.: Implementation of a 1-D thermodynamic model for simulating the wintertime evolvement of physical properties of snow and ice over the Arctic Ocean, J. Adv. Model. Earth Sy., 13, e2020MS002448, https://doi.org/10.1029/2020MS002448, 2021.

Kang, E.-J., Sohn, B.-J., Tonboe, R. T., Noh, Y.-C., Kwon, I.-H., Kim, S.-W., Maturilli, M., Kim, H.-C., and Liu, C.: Explicitly determined sea ice emissivity and emission temperature over the Arctic for surface-sensitive microwave channels, Q. J. Roy. Meteor. Soc., 149, 2011–2030, https://doi.org/10.1002/qj.4492, 2023.

Kang, E.-J., Sohn, B.-J., Song, H.-J., and Liu, C.: Satellite-estimated microwave emissivity and emission temperature over the Arctic sea ice: ANN-based algorithm, J. Geophys. Res.-Atmos., 130, e2024JD042265, https://doi.org/10.1029/2024JD042265, 2025.

https://doi.org/10.5194/essd-2026-471
Preprint. Discussion started: 24 August 2026

Open Access Earth System Science Data Discussions

Kang, E.-J., Sohn, B.-J., Kim, W., Kwon, I.-H., Lee, S., Song, H.-J., and Noh, Y.-C.: Impact of satellite-based ice skin temperature initialization on Arctic winter forecasts using the Korean Integrated Model, Geosci. Lett., 13, 1, https://doi.org/10.1186/s40562-025-00450-1, 2026.

Kang, E.-J.: AMSR2 penetration-aware Arctic sea-ice emissivity and emission temperature dataset, 2012–2025, Version 1, Zenodo [data set], https://tinyurl.com/5n6843r8 (shortened link redirecting to https://zenodo.org/records/19491578?preview=1&token=eyJhbGciOiJIUzUxMiJ9.eyJpZCI6IjYyMmZiYzE0LTJiMjEtNDE5ZS1hNjNkLTRmYjViMDFhY2I4NiIsImRhdGEiOnt9LCJyYW5kb20iOiI3MWU4MGM1MTgwNDFkNmU2OGYyNWQxZGM1MDVhODUwOCJ9.ZPjK400g8JIYY_6MqIytp3U_Q9oALZq6Ou70-LBsC7UWIVBeokVIklOLC9IITоKILU6WPQ5ILKf_Xsl8Q_Yoag; last access: 11 August 2026), 2026.

Karbou, F., Rabier, F., and Prigent, C.: The assimilation of observations from the Advanced Microwave Sounding Unit over sea ice in the French global numerical weather prediction system, Mon. Weather Rev., 142, 125–140, https://doi.org/10.1175/MWR-D-13-00025.1, 2014.

Kern, S., Lavergne, T., Notz, D., Pedersen, L. T., Tonboe, R. T., Saldo, R., and Sørensen, A. M.: Satellite passive microwave sea-ice concentration data set intercomparison: closed ice and ship-based observations, The Cryosphere, 13, 3261–3307, https://doi.org/10.5194/tc-13-3261-2019, 2019.

Kilic, L., Jimenez, C., Prigent, C., Korosov, A., Rampal, P., de Gélis, I., and Garric, G.: Parameterization of the winter Arctic sea ice microwave emissivity between 1.4 and 36 GHz, for large scale applications, Earth Space Sci., 12, e2025EA004259, https://doi.org/10.1029/2025EA004259, 2025.

Kim, J.-M., Sohn, B.-J., Lee, S.-M., Shi, H., Kwon, Y.-J., Kim, S.-W., and Kim, H.-C.: The estimation of the total freeboard of Arctic sea ice in winter using passive microwave satellite measurements, J. Atmos. Ocean. Tech., 39, 1611–1627, https://doi.org/10.1175/JTECH-D-21-0105.1, 2022.

Kim, J.-S., Ahn, M.-H., and Lee, S.-M.: A new bias correction approach for better assimilation of microwave sounding data over winter sea ice in the Korean Integrated Model, IEEE T. Geosci. Remote, 61, 4108212, https://doi.org/10.1109/TGRS.2023.3335930, 2023.

Kojima, K.: Densification of seasonal snow cover, Physics of Snow and Ice: Proceedings, 1, 929–952, Institute of Low Temperature Science, Hokkaido University, Sapporo, Japan, https://hdl.handle.net/2115/20351 (last access: 4 June 2026), 1967.

Kummerow, C. D., Berg, W. K., Kuo, C.-P., and NOAA CDR Program: NOAA Climate Data Record (CDR) of SSMI(S) and AMSR2 microwave brightness temperatures, CSU Version 2, NOAA National Centers for Environmental Information [data set], https://doi.org/10.25921/E3K5-BW77, 2022.

Lavergne, T., Eastwood, S., Teffah, Z., Schyberg, H., and Breivik, L.-A.: Sea ice motion from low-resolution satellite sensors: An alternative method and its validation in the Arctic, J. Geophys. Res.-Oceans, 115, C10032, https://doi.org/10.1029/2009JC005958, 2010.

Lavergne, T., Sørensen, A. M., Kern, S., Tonboe, R., Notz, D., Aaboe, S., Bell, L., Dybkjær, G., Eastwood, S., Gabarro, C., Heygster, G., Killie, M. A., Kreiner, M. B., Lavelle, J., Saldo, R., Sandven, S., and Pedersen, L. T.: Version 2 of the EUMETSAT OSI SAF and ESA CCI sea-ice concentration climate data records, The Cryosphere, 13, 49–78, https://doi.org/10.5194/tc-13-49-2019, 2019.

Lavergne, T., Kern, S., Aaboe, S., Derby, L., Dybkjaer, G., Garric, G., Heil, P., Hendricks, S., Holfort, J., Howell, S., Key, J., Lieser, J. L., Maksym, T., Maslowski, W., Meier, W., Muñoz-Sabater, J., Nicolas, J., Özsoy, B., Rabe, B., Rack, W., Raphael, M., de Rosnay, P., Smolyanitsky, V., Tietsche, S., Ukita, J., Vichi, M., Wagner, P., Willmes, S., and Zhao, X.: A new structure for the sea ice essential climate variables of the Global Climate Observing System, B. Am. Meteorol. Soc., 103, E1502–E1521, https://doi.org/10.1175/BAMS-D-21-0227.1, 2022.

Lawrence, H., Bormann, N., Sandu, I., Day, J., Farnan, J., and Bauer, P.: Use and impact of Arctic observations in the ECMWF Numerical Weather Prediction system, Q. J. Roy. Meteor. Soc., 145, 3432–3454, https://doi.org/10.1002/qj.3628, 2019.

Lee, S.-M., Sohn, B.-J., and Kim, S.-J.: Differentiating between first-year and multiyear sea ice in the Arctic using microwave-retrieved ice emissivities, J. Geophys. Res.-Atmos., 122, 5097–5112, https://doi.org/10.1002/2016JD026275, 2017.

Maeda, T., Taniguchi, Y., and Imaoka, K.: GCOM-W1 AMSR2 level 1R product: Dataset of brightness temperature modified using the antenna pattern matching technique, IEEE T. Geosci. Remote, 54, 770–782, https://doi.org/10.1109/TGRS.2015.2465170, 2016.

Marbouty, D.: An experimental study of temperature-gradient metamorphism, J. Glaciol., 26, 303–312, https://doi.org/10.3189/S0022143000010844, 1980.

Mathew, N., Heygster, G., and Melsheimer, C.: Surface emissivity of the Arctic sea ice at AMSR-E frequencies, IEEE T. Geosci. Remote, 47, 4115–4124, https://doi.org/10.1109/TGRS.2009.2023667, 2009.

https://doi.org/10.5194/essd-2026-471
Preprint. Discussion started: 24 August 2026

Meier, W. N., Windnagel, A., and Stewart, S.: Sea Ice Concentration: Climate Algorithm Theoretical Basis Document (C-ATBD), NOAA Climate Data Record Program CDRP-ATBD-0107, Revision 11, National Oceanic and Atmospheric Administration, https://www.ncei.noaa.gov/pub/data/sds/cdr/CDRs/Sea_Ice_Concentration/AlgorithmDescription_01B-11.pdf (last access: 8 April 2026), 2024.

Nakata, K., Ohshima, K. I., and Nihashi, S.: Estimation of thin-ice thickness and discrimination of ice type from AMSR-E passive microwave data, IEEE T. Geosci. Remote, 57, 263–276, https://doi.org/10.1109/TGRS.2018.2853590, 2019.

Nicolaus, M., Perovich, D. K., Spreen, G., Granskog, M. A., von Albedyll, L., Angelopoulos, M., Anhaus, P., Arndt, S., Belter, H. J., Bessonov, V., Birnbaum, G., Brauchle, J., Calmer, R., Cardellach, E., Cheng, B., Clemens-Sewall, D., Dadic, R., Damm, E., de Boer, G., Demir, O., Dethloff, K., Divine, D. V., Fong, A. A., Fons, S., Frey, M. M., Fuchs, N., Gabarró, C., Gerland, S., Goessling, H. F., Gradinger, R., Haapala, J., Haas, C., Hamilton, J., Hannula, H.-R., Hendricks, S., Herber, A., Heuzé, C., Hoppmann, M., Høyland, K. V., Huntemann, M., Hutchings, J. K., Hwang, B., Itkin, P., Jacobi, H.-W., Jaggi, M., Jutila, A., Kaleschke, L., Katlein, C., Kolabutin, N., Krampe, D., Kristensen, S. S., Krumpen, T., Kurtz, N., Lampert, A., Lange, B. A., Lei, R., Light, B., Linhardt, F., Liston, G. E., Loose, B., Macfarlane, A. R., Mahmud, M., Matero, I. O., Maus, S., Morgenstern, A., Naderpour, R., Nandan, V., Niubom, A., Oggier, M., Oppelt, N., Pätzold, F., Perron, C., Petrovsky, T., Pirazzini, R., Polashenski, C., Rabe, B., Raphael, I. A., Regnery, J., Rex, M., Ricker, R., Riemann-Campe, K., Rinke, A., Rohde, J., Salganik, E., Scharien, R. K., Schiller, M., Schneebeli, M., Semmling, M., Shimanchuk, E., Shupe, M. D., Smith, M. M., Smolyanitsky, V., Sokolov, V., Stanton, T., Stroeve, J., Thielke, L., Timofeeva, A., Tonboe, R. T., Tavri, A., Tsamados, M., Wagner, D. N., Watkins, D., Webster, M., and Wendisch, M.: Overview of the MOSAiC expedition: Snow and sea ice, Elementa: Science of the Anthropocene, 10, 000046, https://doi.org/10.1525/elementa.2021.000046, 2022.

Numerical Weather Prediction Satellite Application Facility (NWP SAF): Radiative Transfer for TOVS [software], https://nwp-saf.eumetsat.int/site/software/rttov/download/ (last access: 4 June 2026).

Ocean and Sea Ice Satellite Application Facility (OSI SAF): Global Sea Ice Type [data set], European Organisation for the Exploitation of Meteorological Satellites, https://doi.org/10.15770/EUM_SAF_OSI_NRT_2006, 2017.

Phalippou, L.: A microwave radiative transfer model, ECMWF Technical Memorandum No. 190, European Centre for Medium-Range Weather Forecasts, https://doi.org/10.21957/0slwcfoqi, 1992.

Prigent, C., Rossow, W. B., and Matthews, E.: Microwave land surface emissivities estimated from SSM/I observations, J. Geophys. Res.-Atmos., 102, 21867–21890, https://doi.org/10.1029/97JD01360, 1997.

https://doi.org/10.5194/essd-2026-471
Preprint. Discussion started: 24 August 2026

Rostosky, P., Stroeve, J. C., Huntemann, M., Kaleschke, L., Nanderpour, R., Spreen, G., and Thielke, L.: Brightness temperature measured by UoM SBR radiometer at 19, 37 and 89 GHz from September 2019 to September 2020 during the MOSAiC expedition, PANGAEA [data set], https://doi.org/10.1594/PANGAEA.956108, 2023.

Saunders, R., Hocking, J., Turner, E., Rayer, P., Rundle, D., Brunel, P., Vidot, J., Roquet, P., Matricardi, M., Geer, A., Bormann, N., and Lupu, C.: An update on the RTTOV fast radiative transfer model (currently at version 12), Geosci. Model Dev., 11, 2717–2737, https://doi.org/10.5194/gmd-11-2717-2018, 2018.

Schanda, E., Matzler, C., and Kunzi, K.: Microwave remote sensing of snow cover, Int. J. Remote Sens., 4, 149–158, https://doi.org/10.1080/01431168308948536, 1983.

Stroeve, J. C., Markus, T., Maslanik, J. A., Cavalieri, D. J., Gasiewski, A. J., Heinrichs, J. F., Holmgren, J., Perovich, D. K., and Sturm, M.: Impact of surface roughness on AMSR-E sea ice products, IEEE T. Geosci. Remote, 44, 3103–3117, https://doi.org/10.1109/TGRS.2006.880619, 2006.

Tonboe, R. T.: The simulated sea ice thermal microwave emission at window and sounding frequencies, Tellus A, 62, 333–344, https://doi.org/10.1111/j.1600-0870.2010.00434.x, 2010.

Tonboe, R. T., Dybkjær, G., and Høyer, J. L.: Simulations of the snow covered sea ice surface temperature and microwave effective temperature, Tellus A, 63, 1028–1037, https://doi.org/10.1111/j.1600-0870.2011.00530.x, 2011.

Ulaby, F. T. and Long, D. G.: Microwave radar and radiometric remote sensing, Artech House, 1116 pp., 2015.

Wang, D., Prigent, C., Kilic, L., Fox, S., Harlow, C., Jimenez, C., Aires, F., Grassotti, C., and Karbou, F.: Surface emissivity at microwaves to millimeter waves over polar regions: Parameterization and evaluation with aircraft experiments, J. Atmos. Ocean. Tech., 34, 1039–1059, https://doi.org/10.1175/JTECH-D-16-0188.1, 2017.

Winebrenner, D. P., Bredow, J., Fung, A. K., Drinkwater, M. R., Nghiem, S., Gow, A. J., Perovich, D. K., Grenfell, T. C., Han, H. C., Kong, J. A., Lee, J. K., Mudaliar, S., Onstott, R. G., Tsang, L., and West, R. D.: Microwave sea ice signature modeling, in: *Microwave Remote Sensing of Sea Ice*, edited by: Carsey, F. D., Geophysical Monograph Series, 68, 137–175, American Geophysical Union, Washington, DC, https://doi.org/10.1029/GM068p0137, 1992.

Worby, A. P. and Comiso, J. C.: Studies of the Antarctic sea ice edge and ice extent from satellite and ship observations, Remote Sens. Environ., 92, 98–111, https://doi.org/10.1016/j.rse.2004.05.007, 2004.